

Telling the spin of the di-photon resonance

Marco Fabbrichesi[†], Michele Pinamonti^{‡*}, and Alfredo Urbano[°]

[†]*INFN, Sezione di Trieste, via Valerio 2, 34136 Trieste, Italy*

[‡]*INFN, Sezione di Trieste, Gruppo collegato di Udine*

^{*}*SISSA, via Bonomea 265, 34136 Trieste, Italy and*

[°]*Theoretical Physics Department, CERN, Geneva, Switzerland*

(Dated: April 26, 2016)

We argue that the spin of the 750 GeV resonance can be determined at the 99.7% confidence level in the di-photon channel with as few as 10 fb^{-1} of luminosity. This result is true if the resonance is produced by gluon fusion (independently of the selection cuts) while an appropriate choice of selection cuts is needed if quark production is sub-dominantly present—which is the case of the Kaluza-Klein gravitational excitation under the hypothesis of a spin-2 resonance. A proportionally larger luminosity is required if the model for the spin-2 resonance includes a dominant production by quarks or in the absence of an efficient separation of the signal from the background.

PACS numbers: 12.60.Cn, 14.80.Rt, 14.80.Ec

I. MOTIVATIONS AND SUMMARY

The presence of a new state—a resonance in the di-photon channel in the first run of the LHC at 13 TeV [1]—will soon be either confirmed or disproved. Meanwhile, the mere possibility of its existence behoves us to look, first and foremost, for the identification of its other properties beside the mass. Only starting from such a full description—inclusive of mass, spin, parity and production and decay channels—it will be possible to begin to sift through the many possibilities of physics beyond the Standard Model (SM) that might account for its existence.

In this paper, we focus on the determination of the spin of such a new particle after its discovery. This problem has been discussed for the Higgs boson by both theorists [2] and experimentalists [3]. It is therefore only a matter of adopting some of these analyses to the present case of a resonance with a mass of about 750 GeV. While a complete study must be based on the simultaneous use of different decays, we restrict ourselves to the di-photon channel because it is here that the resonance has been seen and will mostly likely be hunted down. In this channel, barring higher spin values, only two possibilities, spin-0 and 2, need to be discussed [4].

While the significance required for a discovery has been set very high at the 5σ level to avoid the risk of spurious results from even very unlikely background fluctuations, once the new particle discovery has been established, the determination of its spin can be accepted at the more mundane value of 3σ (99.7% confidence level), as done, for example, for the Higgs boson itself [3].

In general, the discrimination between different spin hypotheses improves if the background can be subtracted in a reliable manner. We discuss *sPlot* [5]—a procedure that provides such a separation—and compare the significance of the spin determination for the signal alone and together with the un-subtracted background.

We use and compare a log likelihood ratio (LLR) and a center-edge asymmetry [6] to discriminate between the possible spin hypotheses. The main uncertainty arises from the systematic error in the definition of the spin-2 model because of the different production mechanisms which have different angular distributions. If we assume that the spin-2 particle is almost completely produced by gluon fusion, it will be possible not only to discover the existence of the new state but also fix its spin with as few as 10 fb^{-1} of luminosity in the di-photon channel. The number of events required for spin discrimination depends on the selection cuts utilised when the spin-2 particle is assumed to be significantly produced also from quarks. We discuss in detail the spin-2 model embodied by the lightest Kaluza-Klein graviton excitation after implementing the current constraints of its couplings to gluon, quark and photons. In this case an appropriated choice of selection cuts makes possible the spin identification again with only 10 fb^{-1} of luminosity. A proportionally larger luminosity is required if the model for the spin-2 resonance includes a dominant production by quarks or in the absence of an efficient separation of the signal from the background.

We conclude by reviewing the potential relevance of terms of interference between signal and background [7] because they may play a role more important for the 750 GeV resonance than in the Higgs boson case.

Two analyses of the 750 di-photon resonance recently appeared in which the issue of the spin determination is discussed. The authors of ref. [8] utilise a framework which cleverly exploits an encoding of the spin properties and production modes in the cross sections. It is an analysis that is different from ours and that can be seen as complementary. The authors of ref. [9] discuss how to characterise the new state by means of distributions of a number of kinematical variables in various decay channels.

II. FIT OF THE INVARIANT MASS DISTRIBUTION

The first step in the analysis consists in extracting from the di-photon invariant mass $m_{\gamma\gamma}$ data the value of the parameters of the models describing signal and background.

We use the most recently published data from the ATLAS collaboration [10] on the distribution of the di-photon mass invariant to fit the parameters of the signal and the background. While comparable data are also available from the CMS collaboration [11], we use those of the ATLAS collaboration because of the higher significance of the signal and their inclusion of the angular distributions in the published results. These experimental angular distributions are discussed in the appendix.

The signal is modelled by a Breit-Wigner distribution

$$f_{\text{BW}}(m_{\gamma\gamma}) = \frac{2\mathcal{N}_{\text{BW}}}{\pi} \left[\frac{\Gamma_X^2 M_X^2}{(m_{\gamma\gamma}^2 - M_X^2)^2 + m_{\gamma\gamma}^4 \Gamma_X^2 / M_X^2} \right]. \quad (1)$$

At this level, models of the resonance with different spin differ only by the overall normalisation of their respective signals and are not distinguishable. Fits of the invariant mass for different spins in the published data refer to differences in the selection cuts. We use the data after the Higgs-like cuts: $E_T^{\gamma 1} > 40 m_{\gamma\gamma}$ GeV, $E_T^{\gamma 2} > 30 m_{\gamma\gamma}$ GeV.

The background is described by a family of nested functions with an increasing number of degrees of freedom

$$f_{(k)}(x; b, a_k) = \mathcal{N}_{\text{BG}} \left(1 - x^{1/3}\right)^b x^{\sum_{j=0}^k a_j (\ln x)^j}, \quad (2)$$

with $x \equiv m_{\gamma\gamma}/\sqrt{s}$ and b, a_j the parameters of the functions.

We perform a maximum likelihood (MLL) fit, the result of which is shown in fig. 1. It nicely agrees with what reported by the experimental collaboration. In table I we collect the best-fitted values and errors thereof.

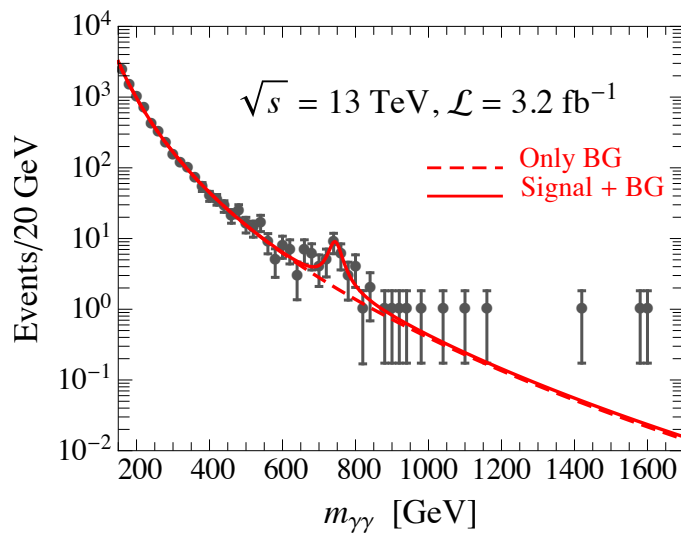


FIG. 1: The fit of the invariant mass distribution with selection cuts: $E_T^{\gamma 1} > 40 m_{\gamma\gamma}$ GeV, $E_T^{\gamma 2} > 30 m_{\gamma\gamma}$ GeV. Data digitally extracted from [10].

A similar procedure can be followed in the case of the data after looser cuts ($E_T^{\gamma 1}$ and $E_T^{\gamma 2} > 55$ GeV). We do not attempt such a fit here because it depends on a non-analytic modelling of the background, and simply rely on the experimental collaboration that gives 25 events for the signal and 45 for the background [10].

This MLL fit provides us with an estimate of the probability that given model B for the background and S for the signal, the data are in agreement with the expectations of having such a signal on top of the background, $P(\text{data}|S+B)$, as opposed to the background alone, $P(\text{data}|B)$. Such an estimate is an example of hypothesis testing and is usually parametrised in terms of a likelihood ratio $\mathcal{L} = -2 \log P(\text{data}|S+B)/P(\text{data}|B)$.

The ATLAS collaboration cites a significance of $\mathcal{Z} = 3.9$ ($\mathcal{Z} = 3.6$) for the fit in what they call “spin-0 (spin-2) analysis” or, which is the same, the probability for the data to be a statistical fluctuation is, for both cases, of the order of or less than 10^{-3} . The different significances for the two analyses are due to the higher background entering the selection in the case of the “spin-2 analysis”—which contains more events in the forward direction where we also find most of the background.

TABLE I: Result of the MLL fit in the invariant mass range from 700 to 840 GeV with selection cuts: $E_T^{\gamma_1} > 40 m_{\gamma\gamma}$ GeV, $E_T^{\gamma_2} > 30 m_{\gamma\gamma}$ GeV. The number of events refers to the signal-plus-background fit.

	Normalisation	Mass [GeV]	Width [GeV]	Normalisation	BG coeff.	BG coeff.
	$\log_{10}(\mathcal{N}_{\text{BW}})$	M_X	Γ_X	$\log_{10}(\mathcal{N}_{\text{BG}})$	a_0	b
Fit	1.04 ± 0.24	745 ± 8	42 ± 27	-1.01 ± 0.07	-3.0 ± 0.5	11.2 ± 4.5
	Signal			Background		
# events	$18.0_{-7.6}^{+13.3}$ ($\sigma_X = 5.6_{-2.4}^{+4.2} \text{ fb}^{-1}$)			$12.4_{-1.9}^{+2.3}$		

III. THEORETICAL INPUTS

Since we look at the di-photon channel, the spin of the resonance cannot be 1 [4].¹ We therefore need only discuss the cases of spin-0 and 2.

A. Spin and angular distributions

Considering the di-photon decay $X_J \rightarrow \gamma\gamma$, informations about the spin J of the decaying resonance X_J can be extracted from the distribution of the photon scattering angle in the Collins-Soper (CS) frame [15] (see fig. 2).

For a spin-0 resonance, we have

$$\frac{1}{N^{\text{spin-0}}} \times \frac{dN^{\text{spin-0}}}{dz} = \frac{1}{2}, \quad (3)$$

with $z \equiv \cos \theta^*$ the cosine of CS scattering angle defined as

$$\cos \theta^* = \frac{\sinh \Delta\eta_{\gamma\gamma}}{\sqrt{1 + \left(\frac{p_T^{\gamma}}{m_{\gamma\gamma}}\right)^2}} \frac{2p_T^{\gamma_1} p_T^{\gamma_2}}{m_{\gamma\gamma}^2}. \quad (4)$$

The photon pair transverse momentum is $p_T^{\gamma\gamma} = \sqrt{(p_T^{\gamma_1})^2 + (p_T^{\gamma_2})^2 + 2p_T^{\gamma_1} p_T^{\gamma_2} \cos \Delta\varphi_{\gamma\gamma}}$, with $\Delta\varphi_{\gamma\gamma}$ the azimuthal angle between the two photons; $\Delta\eta_{\gamma\gamma}$ is the pseudo-rapidity difference $\eta_{\gamma_1} - \eta_{\gamma_2}$.

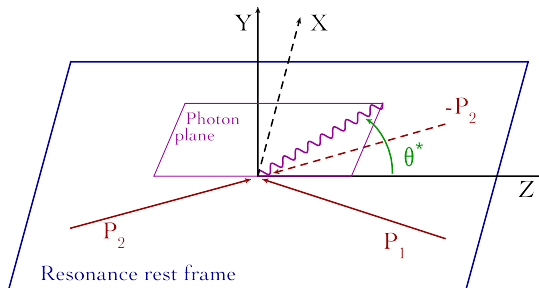


FIG. 2: Pictorial representation of the CS frame. The CS frame is constructed by boosting the event to the resonance's rest frame, and defining the Z-axis as the inner bisector of the two partonic momenta P_1 and $-P_2$ (which are no longer collinear in the resonance's rest frame). The X-axis becomes the outer bisector. The photon scattering angle θ^* is measured w.r.t. the Z-axis.

¹ To avoid this theorem one must add an epicycle and assume that the putative spin 1 resonance decays into a photon and a scalar state which then decays into two almost collinear photons.

For a spin-2 resonance the production mode affects the angular distribution of the final state photons and we have two possibilities:

$$\frac{1}{N_{gg}^{\text{spin}-2}} \times \frac{dN_{gg}^{\text{spin}-2}}{dz} = \frac{5}{32} (1 + 6z^2 + z^4) , \quad (5)$$

$$\frac{1}{N_{qq}^{\text{spin}-2}} \times \frac{dN_{qq}^{\text{spin}-2}}{dz} = \frac{5}{8} (1 - z^4) . \quad (6)$$

In the presence of both production mechanisms the expected angular distribution is

$$\frac{1}{N^{\text{spin}-2}} \times \frac{dN^{\text{spin}-2}}{dz} = \frac{5}{32} (1 + 6z^2 + z^4) (1 - f_{qq}) + \frac{5}{8} (1 - z^4) f_{qq} , \quad (7)$$

where $f_{qq} \equiv N_{qq}^{\text{spin}-2}/N^{\text{spin}-2}$ is the relative weight of the production by quarks.

The two eqs. (5)–(6) show the main problem with any model of a spin-2 resonance: while the gluon production has an angular distribution that is clearly distinguishable from that of spin-0, the case of quark production has an angular distribution rather similar to the spin-0 case and therefore the separation between the two models is more difficult.

The angular distributions in eqs. (3, 5, 6) are strictly valid only considering parton-level events without showering and detector simulation. They are considerably distorted once detector acceptances are included. It is therefore important to investigate the angular distributions in a more complete framework.

The total cross section for the resonant process $pp \rightarrow X_J \rightarrow \gamma\gamma$ is given, in full generality, by

$$\sigma(pp \rightarrow X_J \rightarrow \gamma\gamma) = \frac{2J+1}{M_{X_J} \Gamma_{X_J}} \left[\sum_{\mathcal{P}} C_{\mathcal{P}\mathcal{P}} \Gamma(X_J \rightarrow \mathcal{P}\mathcal{P}) \right] \Gamma(X_J \rightarrow \gamma\gamma) , \quad (8)$$

$C_{\mathcal{P}\mathcal{P}}$ are the dimensionless partonic integrals whose numerical values can be found, for instance, in [12]. Production mechanism and decay modes depends on the microscopic interactions of the resonance.

We do not focus on any particular model and do not attempt to construct the most general effective field theory of the resonance X . In this paper, we only look at those effective interactions that are relevant to determine the spin of the resonance.

B. Spin-0

We assume the following effective interaction Lagrangian

$$\mathcal{L}_{\text{spin}-0} = -\frac{1}{4\Lambda} \left(\kappa_{X_0 WW} W_{\mu\nu}^A W^{A\mu\nu} + \kappa_{X_0 \gamma\gamma} A_{\mu\nu} A^{\mu\nu} + \kappa_{X_0 gg} G_{\mu\nu}^a G^{a\mu\nu} \right) , \quad (9)$$

where $A_{\mu\nu}$, $W_{\mu\nu}^A$, and $G_{\mu\nu}^a$ are the field strength tensors for the SM gauge groups $U(1)_Q$, $SU(2)_L$, and $SU(3)_C$, respectively. We do not introduce any interactions with SM quarks, since the angular distribution in eq. (3) does not depend on the detail of the production mechanism. From eq. (9) we extract the following decay widths

$$\Gamma(X_0 \rightarrow \gamma\gamma) = \frac{\kappa_{X_0 \gamma\gamma}^2 M_{X_0}^3}{64\pi\Lambda^2} , \quad \Gamma(X_0 \rightarrow gg) = \frac{\kappa_{X_0 gg}^2 M_{X_0}^3}{8\pi\Lambda^2} . \quad (10)$$

We show the relevant parameter space in the left panel of fig. 3 in which we fixed $\Lambda = 10$ TeV. The regions shaded in orange corresponds to $\sigma(pp \rightarrow X_0 \rightarrow \gamma\gamma) = [4 - 10]$ fb at $\sqrt{s} = 13$ TeV, that is the value needed to fit the observed excess. According to the result of the fit in section II, we set the total decay width $\Gamma_{X_0} = 42$ GeV and we take $M_{X_0} = 745$ GeV for the mass. We also show in the left panel of fig. 3 the bounds from data at $\sqrt{s} = 8$ TeV. The most relevant constraints come from di-jet and di-photon searches [12, 13].

C. Spin-2

We assume the following interaction effective Lagrangian

$$\mathcal{L}_{\text{spin}-2} = -\frac{1}{\Lambda} \sum_{f=q,l} \kappa_{X_2 ff} T_{\mu\nu}^f X_2^{\mu\nu} - \frac{1}{\Lambda} \sum_{V=Z,W,\gamma,g} \kappa_{X_2 VV} T_{\mu\nu}^V X_2^{\mu\nu} , \quad (11)$$

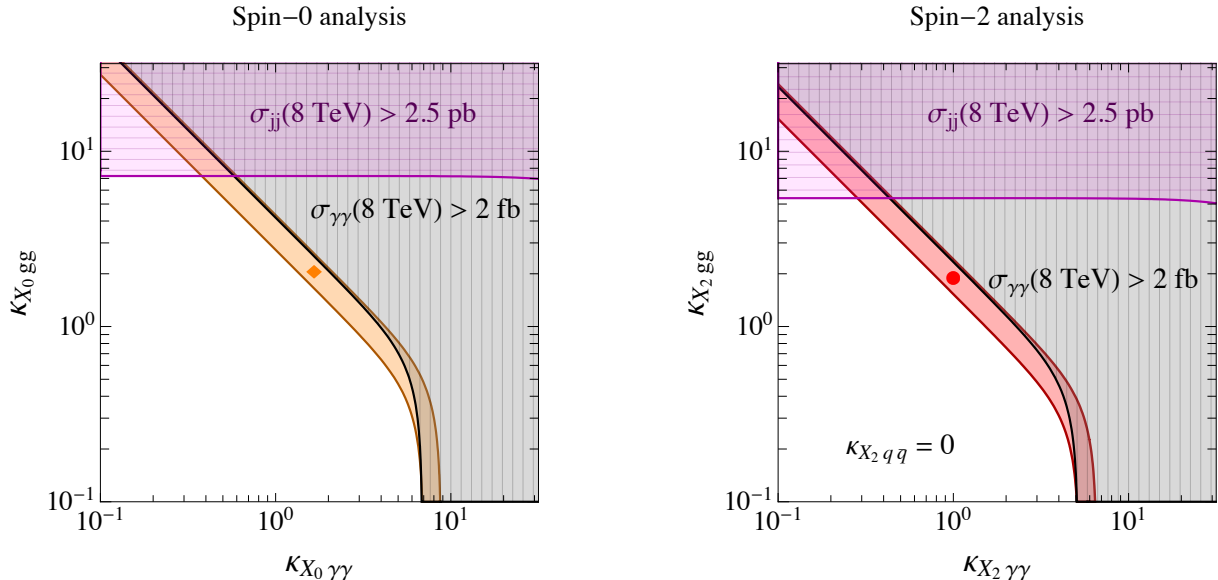


FIG. 3: Constraints on the parameters from data at 8 TeV [12]. The left (right) panel refers to the case of a spin-0 (spin-2) resonance. The regions shaded in orange and red correspond to $\sigma(pp \rightarrow X_J \rightarrow \gamma\gamma) = [4 - 10]$ fb at $\sqrt{s} = 13$ TeV. The orange diamond and red circle correspond to the specific values of the couplings used in section IV.

where the explicit expression for the various components of the energy-momentum tensor can be found in [16]. In full generality we keep separate coupling parameters $\kappa_{X_2 f \bar{f}}$ and $\kappa_{X_2 V V}$ with SM fermions and gauge bosons. In the minimal Randall-Sundrum scenario the couplings of the spin-2 particle—identified with the lightest Kaluza-Klein (KK) graviton excitation—are universal [14].

The case of the KK graviton will be explored in section VI. In order to better illustrate our methodology, and facilitate the comparison with the spin-0 case, we start our discussion from a very simple phenomenological toy model in which all the interactions in eq. (11) but the couplings with photons and gluons are set to zero. In this setup the relevant decay widths are the following

$$\Gamma(X_2 \rightarrow \gamma\gamma) = \frac{\kappa_{X_2 \gamma\gamma}^2 M_{X_2}^3}{80\pi\Lambda^2}, \quad \Gamma(X_2 \rightarrow gg) = \frac{\kappa_{X_2 gg}^2 M_{X_2}^3}{10\pi\Lambda^2}. \quad (12)$$

In this case we expect to reproduce the angular distribution given in eq. (5), and the differences between spin-0 and spin-2 are therefore maximised.

We show the relevant parameter space in the right panel of fig. 3. As before, we impose for the total decay width $\Gamma_{X_2} = 42$ GeV and we take $M_{X_2} = 745$ GeV.

The case of a narrow width is not excluded by current data. A resonance with mass M_X and narrow width Γ_X , in fact, inherits—at the level of detector simulation—an effective width comparable with the energy resolution of the detector at invariant mass $m_{\gamma\gamma} \approx M_X$, that is roughly 8 GeV at $m_{\gamma\gamma} \approx 750$ GeV. As we shall discuss in section VI, the KK graviton falls into this class of models.

IV. METHODS

A. Background and signal

The irreducible background is comprised of tree-level non-resonant di-photon quark annihilation (diagram A in fig. 4). Due to the t - and u -channel exchange of light quarks, this process is peaked in the forward direction in the relevant invariant mass range. This is not true at lower invariant masses—like those for the analysis of the Higgs boson—where the background shows a different angular distribution.

One-loop gluon fusion into di-photon final state (diagram E in fig. 4) also contributes to the irreducible background. The gluon fusion process competes with the tree-level quark annihilation for photon pairs of invariant mass less than 200 GeV [17] where the loop suppression is compensated by (in order of importance) the large gluon luminosity, the accidentally large value of the scattering amplitude, and the coherent sum of all quark flavors in the loop. In the

invariant mass range $m_{\gamma\gamma} = [700 - 840]$ GeV, on the contrary, the one-loop gluon fusion process turns out to be suppressed with respect to the tree-level quark annihilation, and therefore largely subdominant for our purposes. We come back to these loop diagrams in the appendix A.

The reducible background is mostly comprised of tree-level quark annihilation into one photon and one gluon (diagram *B* in fig. 4) and two gluons (diagram *C* in fig. 4) in the final state. These processes mimic the di-photon final state because of possible misidentification of gluons at the detector level.

In our simulations we focus only on the irreducible $q\bar{q} \rightarrow \gamma\gamma$ background. As shown in detail in [10] the reducible background component generated from the probability for a jet to fake a photon is subdominant with respect to the genuine di-photon pair production in the whole invariant mass range $m_{\gamma\gamma} = [200 - 2000]$ GeV.

The signal is generated by s -channel resonant production of X (diagram *D* in fig. 4, in the case of spin-2 resonance produced via gluon fusion) with subsequent di-photon decay. We implement the Lagrangian in eqs. (9,11) in `FeynRules` [18] following the benchmark example of the Higgs characterisation model [19].

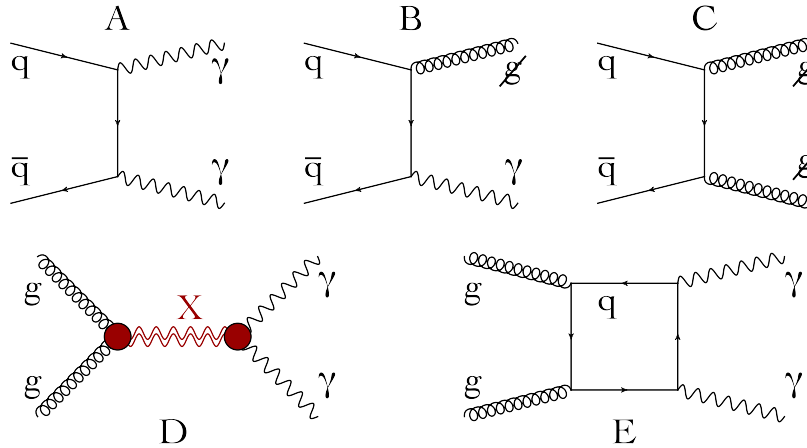


FIG. 4: Representative Feynman diagrams for background and signal.

We generate background, signal, and background-plus-signal samples by means of the matrix-element plus parton-shower merging procedure. We use `MadGraph5_aMC@NLO` [20] (MG5 hereafter) supplemented by `Pythia6` [21] for showering and `Delphes` [22] for detector simulations. We generate signal samples via $pp \rightarrow X_{0,2} \rightarrow \gamma\gamma$, and we add processes with additional 1 and 2 jets matching the correct parton multiplicity using the MLM algorithm. The merging separation parameter is set to $Q_{\text{cut}} = 200$ GeV. Irreducible background as well as signal-plus-background samples are generated following the same procedure.

B. Selection cuts

Only events within the interval $m_{\gamma\gamma} = [700-840]$ GeV are considered. A first cut is enforced on the rapidity and, following [10], the region $|\eta| > 2.37$ as well as the window $\eta = [1.37 - 1.52]$ are excluded.

Mainly for historical reasons, the analysis of the spin has been presented by the experimental collaborations with two different selection cuts in the transverse energy. In a perhaps misleading labelling, they have been referred to as “spin-0” and “spin-2 analysis”. We rename them. The first one (*tight cuts*) are like those used for the study of the Higgs boson. The other set (*loose cuts*) allow for lower values of p_T and populate the forward region.

The two sets are

$$\text{tight selection cuts: } (E_T^{\gamma_1} > 0.4 m_{\gamma\gamma}, E_T^{\gamma_2} > 0.3 m_{\gamma\gamma}), \quad (13)$$

and

$$\text{loose selection cuts: } (E_T^{\gamma_1} > 55 \text{ GeV}, E_T^{\gamma_2} > 55 \text{ GeV}). \quad (14)$$

The tight cuts remove most of the forward region, a region where acceptance effects are important. Moreover, having the spin-0 case in mind, these cuts were devised to reduce the contribution of the the background which is mostly in this region. Notice that the tight cuts have the additional nice feature of reducing the correlation between the invariant mass and the angular distribution. On the other hand, the loose cuts were thought with the case of a

spin-2 state in mind because of its angular distribution that, at least in the case of gluon production, peaks in the forward direction.

We consider both selection cuts and compare their effectiveness.

C. Unfolding the data with $sPlot$

In our analysis we assume that an effective way of separating the signal from the background has been implemented. This is a complicated problem with many subtle implications and different solutions. We illustrate this crucial step by means of $sPlot$ [5], a technique that makes it possible to unfold the data and isolate the signal. This technique allows to reconstruct the distribution of a *control* variable by means of our knowledge of the *discriminating* variable distribution. It is useful in those cases in which we know how to separate the signal from the background for the discriminating variable better than for the control variable.

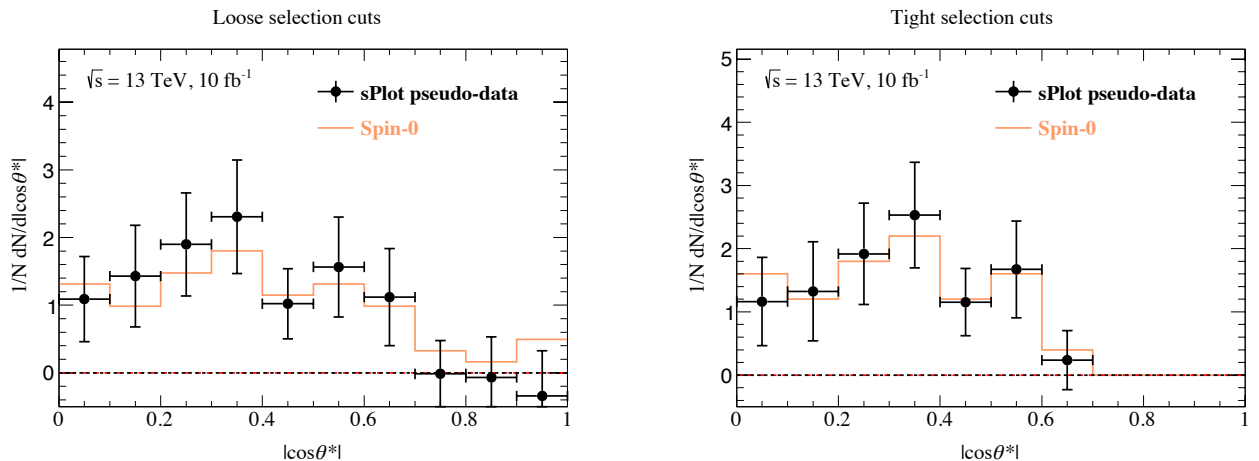


FIG. 5: Pseudo-data of angular distribution of the signal after unfolding by means of $sPlot$ compared with the Monte Carlo generated spin-0 signals for a 10 fb^{-1} luminosity.

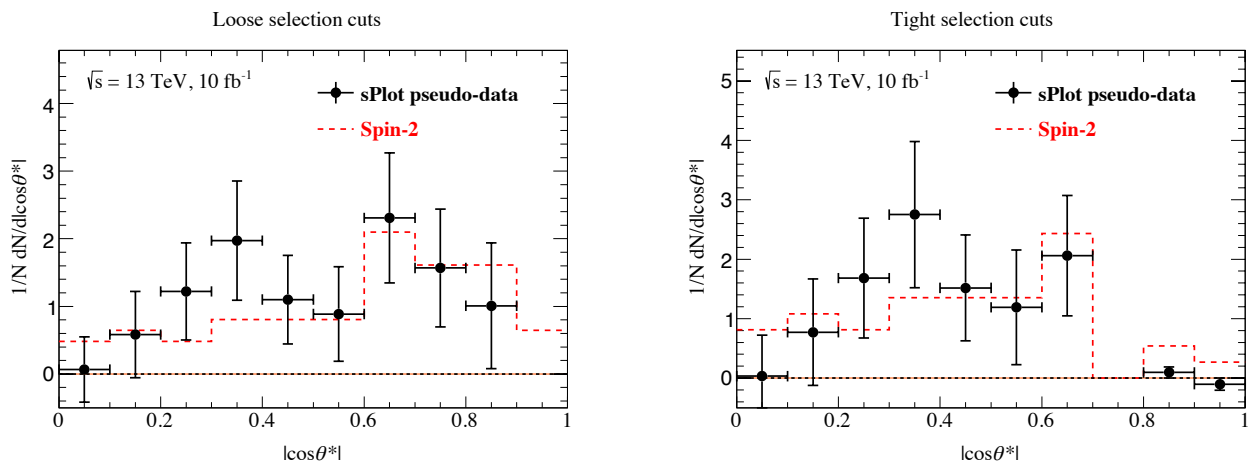


FIG. 6: Pseudo-data of angular distribution of the signal after unfolding by means of $sPlot$ compared with the the Monte Carlo generated spin-2 signals for a 10 fb^{-1} luminosity.

The technique can be summarised as follows. Given a likelihood for N_e events in which the events for the signal

N_S and the background N_B are mixed:

$$\mathcal{L} = \sum_{k=1}^{N_e} \ln [N_S \times \text{pdf}_S(x_k) + N_B \times \text{pdf}_B(x_k)] - N_S - N_B, \quad (15)$$

one computes first the *sWeights*

$${}_sW_n(x_k) = \frac{\mathbf{V}_n^S \times \text{pdf}_S(x_k) + \mathbf{V}_n^B \times \text{pdf}_B(x_k)}{\hat{N}_S \times \text{pdf}_S(x_k) + \hat{N}_B \times \text{pdf}_B(x_k)}, \quad (16)$$

where $\hat{N}_{S,B}$ maximises the likelihood \mathcal{L} and $(\mathbf{V}_n^{S,B})^{-1} = -\partial^2 \mathcal{L} / \partial N_n \partial N_{S,B}$. The discriminating variable x_k is in our case $m_{\gamma\gamma}$, the di-photon invariant mass.

The histograms for the control variable y_k —in our case $\cos \theta$ in the bin k —are then generated by computing

$$\bar{y}_n = \sum_{|y_k - \bar{y}_n| < \delta_y} {}_sW_n(x_k), \quad (17)$$

where δ_y and \bar{y}_k are, respectively, the width and central value of the control variable in the given bin. The histogram constructed from this prescription is called the *sPlot* and provides us with the angular distribution of the signal independently of the background events.

The method works best if control and discriminating variables are uncorrelated—as they mostly are in the case of invariant mass and angular variables, with some dependence, as already discussed, on the selection cuts.

sPlot has been implemented within *Root* [23] and its use already championed in the case of the Higgs boson [2]. Figs. 5 and 6 show the pseudo-data of angular distribution of the signal after unfolding by means of *sPlot* compared with the Monte Carlo generated spin-0 and spin-2 signals for a 10 fb^{-1} luminosity. The error bars and the reliability of the technique improve for higher luminosities.

V. RESULTS

After generating background and signals, we can construct probability density functions (pdf) for both angular and mass invariant distributions. The two spin hypotheses can then be discriminated by measuring either a LLR or an asymmetry on randomly generating events weighted by the angular pdf.

A. Probability density functions

In fig. 7 (fig. 8) we show the pdf's for the tight (loose) selection cuts. The left (right) panels refer to the spin-0 (spin-2) signal hypothesis. We focus on the signal region with invariant mass $m_{\gamma\gamma} = [700 - 840] \text{ GeV}$, and we compare angular distributions for signal (dotted lines), background (dashed lines) and signal-plus-background (solid lines) simulated events.

As already discussed, the tight selection cuts have the effect of suppressing the forward region with $|\cos \theta^*| \gtrsim 0.7$. On the contrary, the loose selection cuts in eq. (14) populate the forward region. This is generally true for background and signals alike irrespective of the spin of the signal. In other words, an enhanced number of events in the forward direction is, by itself, only the effect of the loosening of the selection cuts and provides no indication about the spin.

B. Log likelihood ratio

The PDFs derived in section V A can be used to test the discriminative power of a LLR between the spin-0 and 2 distributions. For a given pdf describing the $\cos \theta^*$ distribution—either signal, background or a mixture of both—it is possible to randomly generate N_{obs} events and compute the LLR

$$2 \log \frac{\mathcal{L}_{\text{spin-0}}}{\mathcal{L}_{\text{spin-2}}}. \quad (18)$$

By repeating this *pseudo-experiment* N_{ps} times, it is possible to construct a sample that can be used to compute the statistical distribution of a certain hypothesis.

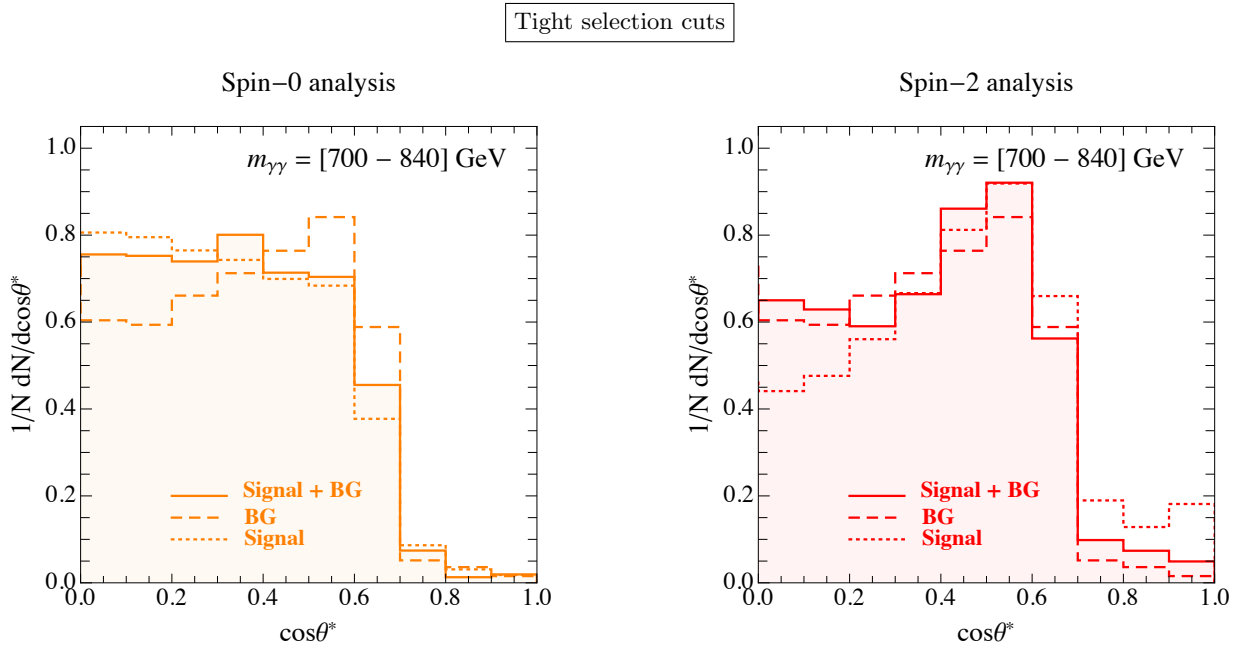


FIG. 7: Angular distributions (normalised to 1 in the interval $\cos\theta^* \in [-1, 1]$) for the tight set of selection cuts for the spin-0 (left panel, orange) and spin-2 (right panel, red) analysis.

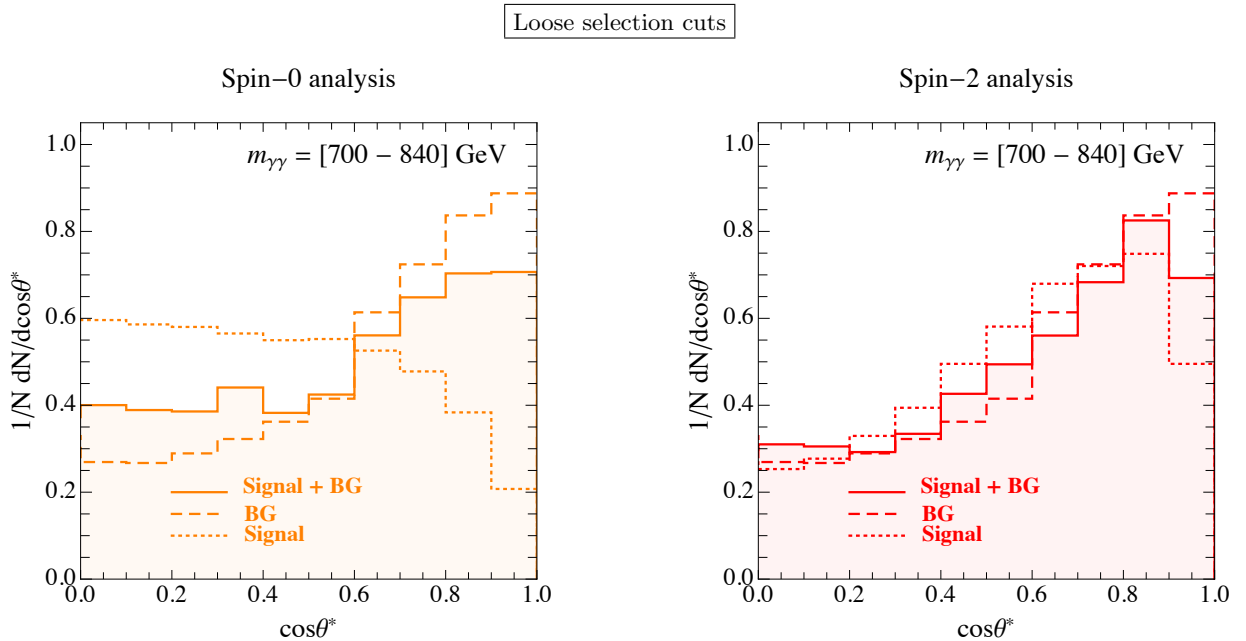


FIG. 8: Angular distributions (normalised to 1 in the interval $\cos\theta^* \in [-1, 1]$) for the loose set of selection cuts for the spin-0 (left panel, orange) and spin-2 (right panel, red) analysis.

Let us take $N_{\text{obs}}^{(J)}$ spin- J signal events generated according to the corresponding pdf (discussed in section V A) as well as $N_{\text{obs}}^{(\text{bkg})}$ events. Each event i is characterised by the value of the cosine of the CS scattering angle z_i defined in eq. (4). The likelihood function for the spin hypothesis J' is given by

$$\mathcal{L}_{\text{spin-}J'} = e^{-N_{\text{obs}}^{(J)} - N_{\text{obs}}^{(\text{bkg})}} \prod_{i=1}^{N_{\text{obs}}^{(J)} + N_{\text{obs}}^{(\text{bkg})}} \left[N_{\text{obs}}^{(J)} \times \text{pdf}_{J'}(z_i) + N_{\text{obs}}^{(\text{bkg})} \times \text{pdf}_{\text{bkg}}(z_i) \right]. \quad (19)$$

As mentioned above, by repeating this measurement N_{ps} time is possible to construct a statistical sample for $\mathcal{L}_{J'}$. We use $N_{ps} = 10^4$.

We follow this prescription and compute the LLR in eq. (18) using the definition in eq. (19). For each of the cases relevant for our analysis (see discussion below) we construct two statistical samples for the ratio $2\log(\mathcal{L}_{\text{spin-0}}/\mathcal{L}_{\text{spin-2}})$: the first one populated with events generated according to the spin-0 distribution, the second one with spin-2 events. We expect the distribution of the ratio $2\log(\mathcal{L}_{\text{spin-0}}/\mathcal{L}_{\text{spin-2}})$ to be peaked at positive values for events generated according to the spin-0 pdf, since in average $\mathcal{L}_{\text{spin-0}} > \mathcal{L}_{\text{spin-2}}$. We expect a distribution peaked towards negative values for events generated according to the spin-2 pdf, since in this case $\mathcal{L}_{\text{spin-0}} < \mathcal{L}_{\text{spin-2}}$.

We explore different cases:

- $N_{\text{obs}}^{(\text{bkg})} = 0$

In this case we consider only signal events. This ideal situation applies to the experimental data after background subtraction. We already stressed in section IV C that this is a complicated task, and we proposed the $sPlot$ technique to tackle the issue. The result obtained in this case should be considered as the case in which the signal has been separated from the background without any loss of information. It is an ideal case that gives the best discrimination one can possibly achieve.

- $N_{\text{obs}}^{(J)} = N_{\text{obs}}^{(\text{bkg})}$

In this case we add to the signal events an equal number of background events. This case captures the impact of the systematic error due to the contamination of the background in the signal sample, as well as the uncertainties in the background modelling.

In each of these two cases we consider the analysis with both tight and loose selection cuts.

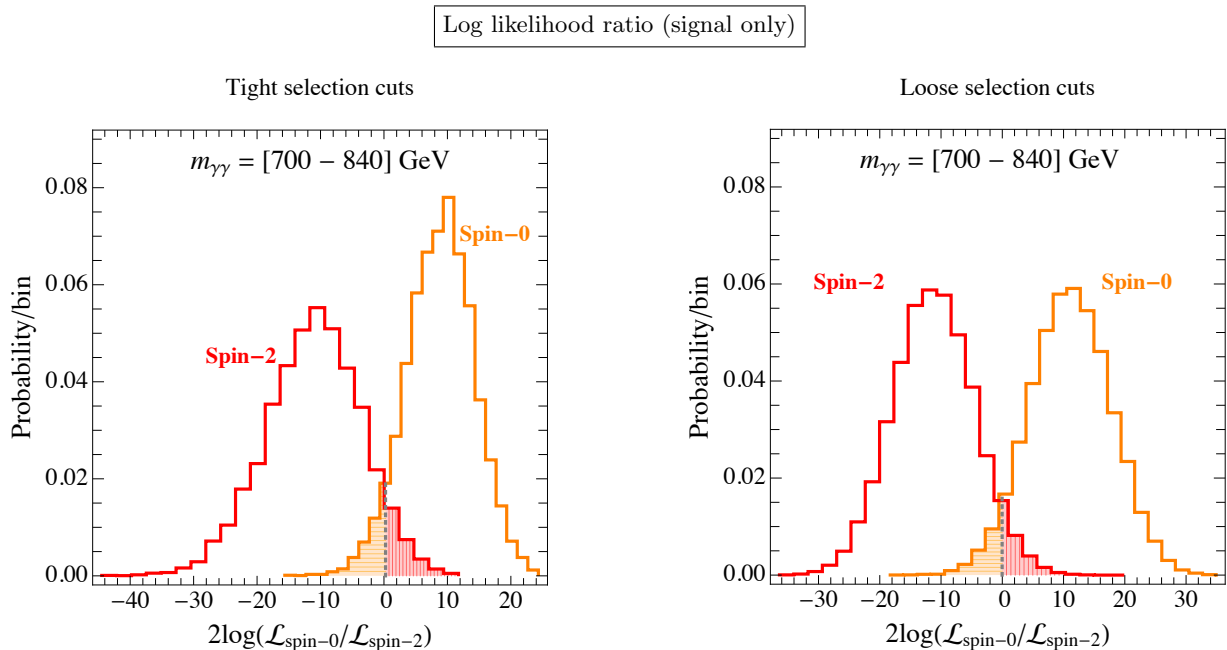


FIG. 9: LLR for $N_{\text{obs}}^{(J)} = 40$ events and $N_{ps} = 10^4$ simulated pseudo-experiments. We show in the left panel (right panel) the analysis with tight selections cuts (loose selection cuts). We included in our Monte Carlo simulation only the distributions for the signal. The vertical grey line marks the point at which the two areas in red (with vertical meshes, for the spin-2 distribution) and orange (with horizontal meshes, for the spin-0 distribution) are equal.

In fig. 9 (fig. 10) we show our results for the LLR analysis considering the case with only signal events (with an equal number of signal and background events). The left (right) panel refers to tight (loose) section cuts. We take $N_{\text{obs}}^{(J)} = 40$ ($N_{\text{obs}}^{(J)} = N_{\text{obs}}^{(\text{bkg})} = 40$) for the analysis with only signal events (with an equal number of signal and background events).

The LLR in figs. 9, 10 take the form of two distinct bell-shaped distributions when computed for the spin-0 and spin-2 hypotheses. To quantify the difference in terms of statistical significance we first compute the point beyond which the right-side tail of the left distribution and the left-side tail of the right one have equal areas. This point

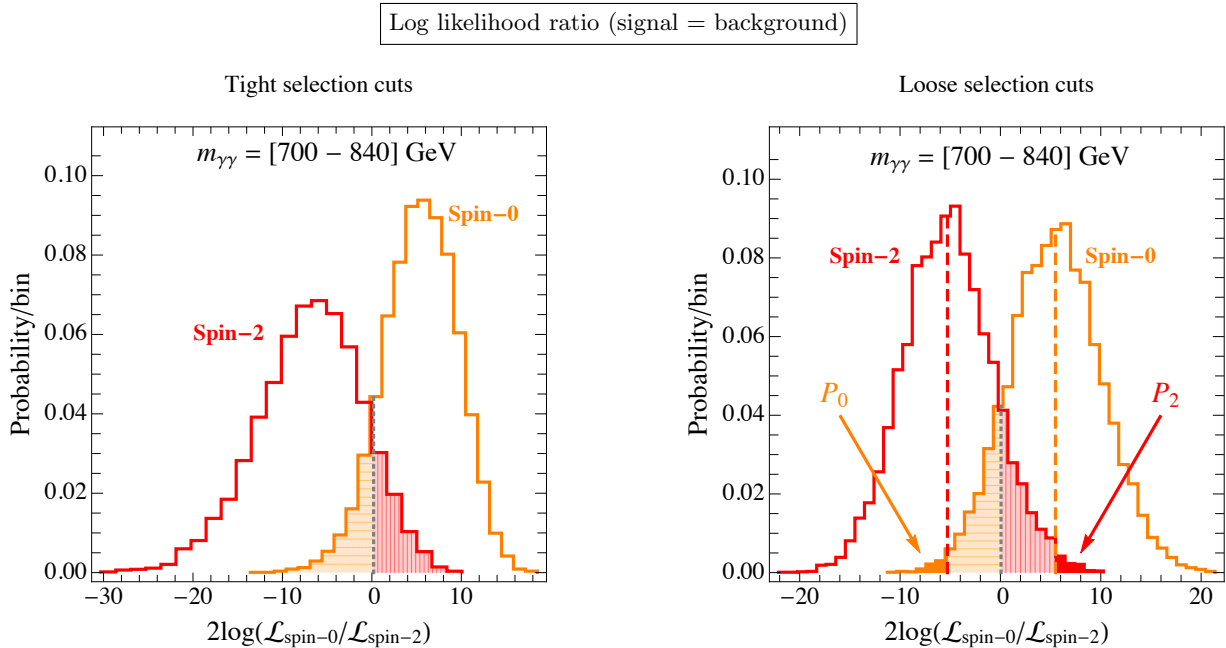


FIG. 10: The same as in fig. 9 but with $N_{\text{obs}}^{(J)} = N_{\text{obs}}^{(\text{bkg})} = 40$ events for both background and signal.

corresponds to a hypothesis test in which no preference for the spin of the resonance is assumed. We mark the point with a vertical dotted grey line. The two equal areas correspond to a p -value which can be translated into a significance \mathcal{Z} as

$$\mathcal{Z} = \Phi^{-1}(1 - p), \quad (20)$$

where

$$\Phi(x) = \frac{1}{2} \left[1 + \text{erf} \left(\frac{x}{\sqrt{2}} \right) \right]. \quad (21)$$

We use the value of \mathcal{Z} to assign a statistical significance to the separation between the two LLR distributions. The significance can be turned into $\mathcal{Z}\sigma$, the number of σ 's, in the approximation in which the distribution is assumed to be Gaussian.

When an actual experiment is performed, a particular value of LLR is obtained. The associated p -value can be computed and the significance of the observation estimated according to the same procedure. For instance, in the right side of fig. 10, the p -value P_0 (P_2) would correspond to a test of the spin-0 (spin-2) hypothesis after the experiment has produced a value close to the corresponding medians. In the approximation of Gaussian distributions, the significance of the given hypothesis corresponds to twice the \mathcal{Z} of the separation.

In fig. 9 the analysis with only signal events allows for a clear separation between the two hypotheses, with the loose selection cuts (right panel) performing slightly better. This is to be expected, since the loose cuts populate the forward region, thus increasing the discriminating power between the two cases. If quantified in terms of the significance \mathcal{Z} introduced before, we find $\mathcal{Z} = 1.56$ ($\mathcal{Z} = 1.67$) for tight (loose) selection cuts. The inclusion of background events reduces the statistical significance of the analysis, and we find $\mathcal{Z} = 1.23$ ($\mathcal{Z} = 1.18$) for tight (loose) selection cuts.

C. Center-edge asymmetry

We define the center-edge asymmetry [6]

$$\mathcal{A}_{CE} \equiv \frac{N_C - N_E}{N_C + N_E}, \quad (22)$$

where N_C (N_E) is the number of events with $-z^* \leq \cos\theta^* \leq z^*$ ($|\cos\theta^*| > z^*$). The parameter z^* is a threshold parameter that can be tuned to optimise the separation between the spin-0 and spin-2 cases.

The analysis for the asymmetry proceed in close analogy with what discussed in the case of the LLR. As before, using the pdf's in section V A we construct two statistical samples for the center-edge asymmetry under the spin-0 and spin-2 hypothesis. Case by case, we can assign a statistical significance using the separation \mathcal{Z} defined in section V B.

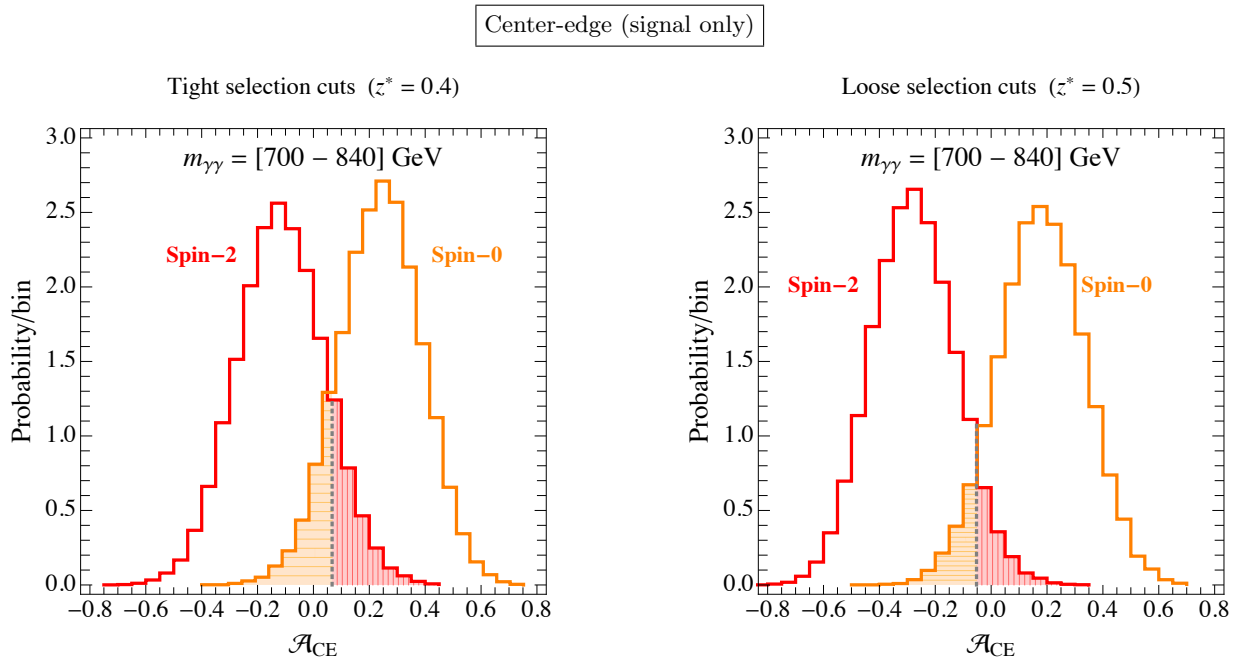


FIG. 11: Central-edge asymmetry distributions for $N_{\text{obs}}^{(J)} = 40$ events and $N_{ps} = 10^4$ simulated pseudo-experiments. We show in the left panel (right panel) the analysis with tight selections cuts (loose selection cuts). We included in our Monte Carlo simulation only the distributions for the signal. The vertical grey line marks the point at which the two areas in red (with vertical meshes, for the spin-2 distribution) and orange (with horizontal meshes, for the spin-0 distribution) are equal.

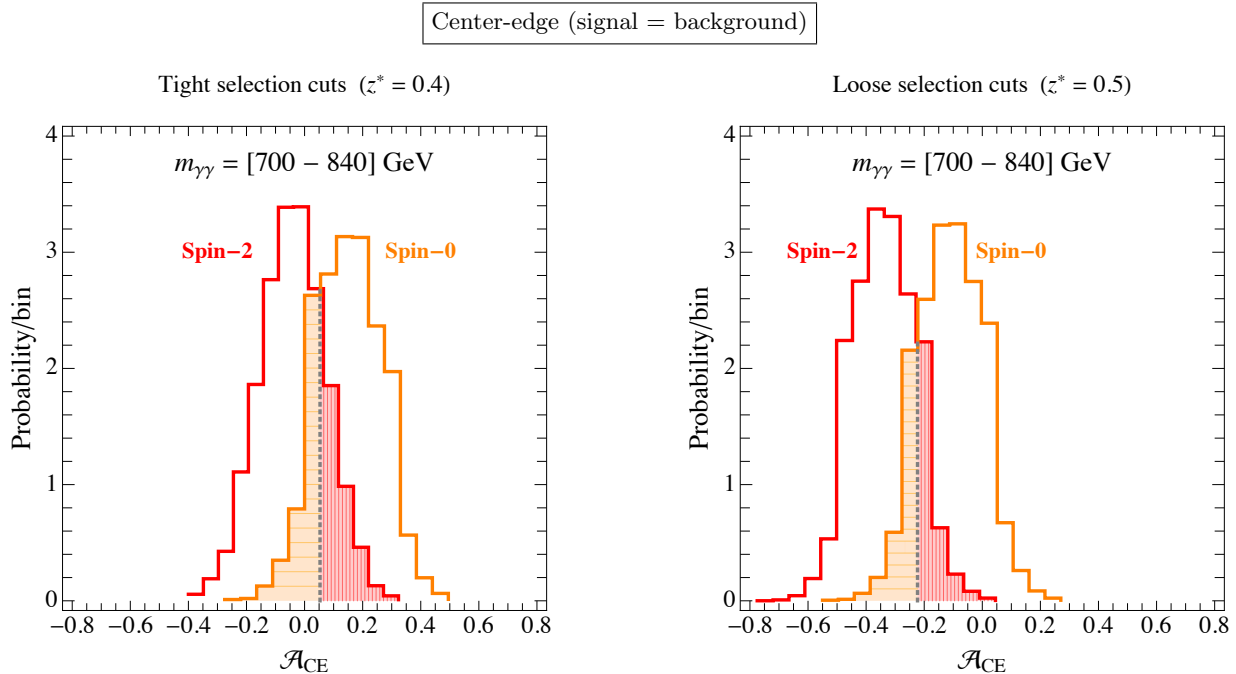


FIG. 12: The same as in fig. 11 but with $N_{\text{obs}}^{(J)} = N_{\text{obs}}^{(\text{bkg})} = 40$ events for both background and signal.

We present our results in fig. 11 (fig. 12) for the case with $N_{\text{obs}}^{(J)} = 40$ signal events (with an equal number of signal

and background events, $N_{\text{obs}}^{(J)} = N_{\text{obs}}^{(\text{bkg})} = 40$). As before, the left (right) panel refers to the analysis with tight (loose) cuts. Furthermore, we find that the value $z^* = 0.4$ is best suited for tight cuts while $z^* = 0.5$ allows for a better separation if loose cuts are imposed.

The medians of the probability distributions in fig. 12 (and the similar ones below) do not correspond to their values at the partonic level—as computed by means of eq. (3) and eqs. (5)–(6)—because of the distortions introduced by the detector.

Considering only signal events, we find the significance $\mathcal{Z} = 1.20$ ($\mathcal{Z} = 1.41$) for tight (loose) selection cuts. Loose selection cuts allow for a better separation between the two spin hypotheses. We notice that the increase in significance gained going from tight to loose cuts is larger for the asymmetry if compared with what found for the LLR. This is because the asymmetry is, by definition, more sensitive to the way in which the events are arranged as a function of the CS angle.

The significance \mathcal{Z} decreases as a consequence of the inclusion of background events, and we find $\mathcal{Z} = 0.80$ ($\mathcal{Z} = 0.98$) for tight (loose) selection cuts. Notice that for loose selection cuts the inclusion of background events shifts the central value of the spin-0 distribution towards negative values. This is because the background, dominated by photon pairs produced in $q\bar{q}$ annihilation, is peaked in the forward region as a consequence of t - and u -channel quark exchange (see figs. 7, 8, right panels). As a result, a large background contamination of the spin-0 signal sample distorts the distribution towards the forward region, and eventually leads to negative values for the central-edge asymmetry—especially if loose cuts are imposed.

D. Significance vs. number of events

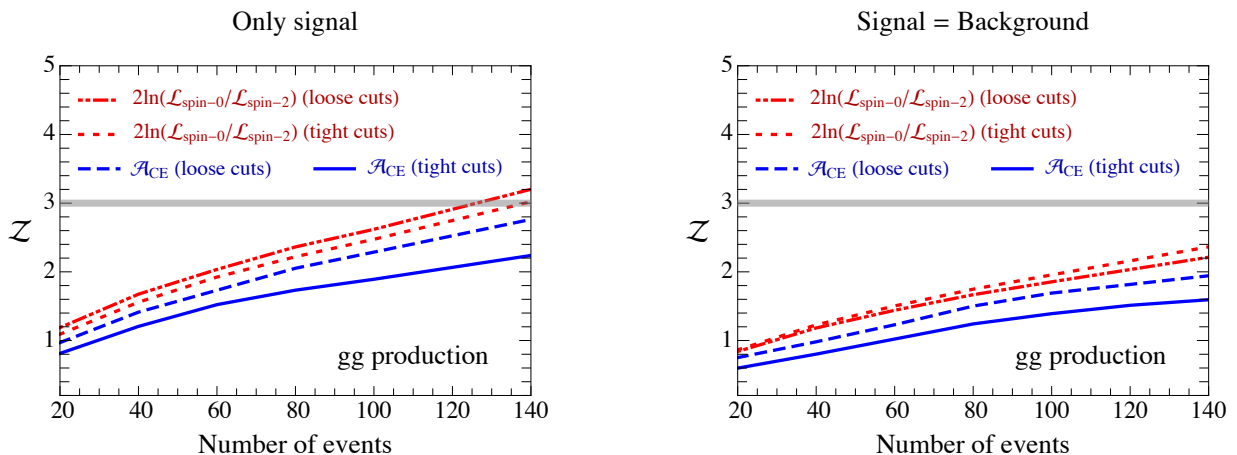


FIG. 13: Significance \mathcal{Z} for the LLR and the center-edge asymmetry as a function of the number of events. In the model for the spin-2 resonance, the production mechanism is taken to be gluon fusion only. In this figure the significance does not refer to one particular spin hypothesis but to the separation between the two distributions (eq. (20) computed with the p-value representing the area equally shared between the two LLRs—see caption of fig. 11). The significance of one particular spin hypothesis—eq. (20) computed with the p-value representing one of the two regions, P_0 or P_2 , in fig. 10—is larger by a factor of 2. This case is discussed in section VI when the spin-2 hypothesis of the KK graviton will be tested.

All the results presented and discussed so far were based on a fixed value of observed events. From a more general perspective, the most valuable information that can be extracted from the analysis is the number of events necessary to reach a certain level of significance \mathcal{Z} in separating the different spin hypotheses. This number is shown in fig. 13 for the two cases, signal only and signal plus background, under discussion. From fig. 13 we see that starting with 60 events and a significance around 2 for the case of LLR on the signal only, we can reach a significance around 3 by simply doubling the number of events. A similar improvement in significance can be seen in the other, less optimal, cases.

Even though a comparison of the two approaches shows (as it should be expected [24]) that the LLR performs roughly 20% better than the central-edge asymmetry, one might bear in mind that the asymmetry is more robust against possible unknown uncertainties and provides a clearer physical picture.

Let us stress that the significance in fig. 13 refers to the separation between the two distributions, and it was computed by means of eq. (20) with the p-value representing the area equally shared between the two LLRs (defined by the gray dashed vertical line in figs. 9-12). The plot in fig. 13 can be used to directly test the two spin hypotheses

by multiplying by a factor of 2 the significance. Assuming an efficient background subtraction and a production of the spin-2 dominated by gluon fusion, roughly 40 events are necessary to reach a significance $\mathcal{Z} = 3$ by means of the LLR. This value is mostly independent of the selection cuts used. Given the cross section value obtained by the fit on the invariant mass distribution in section II—this number of events corresponds to a luminosity of around 5 (7) fb^{-1} after loose (tight) selection cuts. Therefore a luminosity of 10 fb^{-1} will make it possible to determine the spin of the new resonance. This is also a luminosity for which the 5σ significance threshold for a discovery has been comfortably crossed.

VI. THE CASE OF THE LIGHTEST KALUZA-KLEIN GRAVITON EXCITATION

Scenarios with extra dimensions generically predict the existence of massive spin-2 particles (G^* hereafter), corresponding to the KK excitations of the graviton. A possible signature of these models (in particular in the presence of strongly-warped extra dimensions at the TeV scale) could be the discovery of a single resonance—the lightest excitation in the KK tower G^* mentioned above—whose phenomenology can be effectively described by its mass and its universal coupling with the SM energy-momentum tensor (see eq. (11)).

The validity of this setup in the light of the 750 GeV excess was discussed in [25] (see also [26] for related works). The situation is summarised in fig. 14 where we show the allowed parameter space (see caption for details). For $M_{G^*} = 750$ GeV the representative di-photon cross-section $\sigma(pp \rightarrow G^* \rightarrow \gamma\gamma) = [4 - 10]$ fb at $\sqrt{s} = 13$ TeV—necessary to fit the observed excess—implies $\Lambda \approx [47 - 74]$ TeV. The corresponding total decay width is $\Gamma_{G^*} \approx [7 - 18]$ MeV. The strongest bound on the model comes from di-lepton data at $\sqrt{s} = 13$ TeV [27]. These bounds refer to

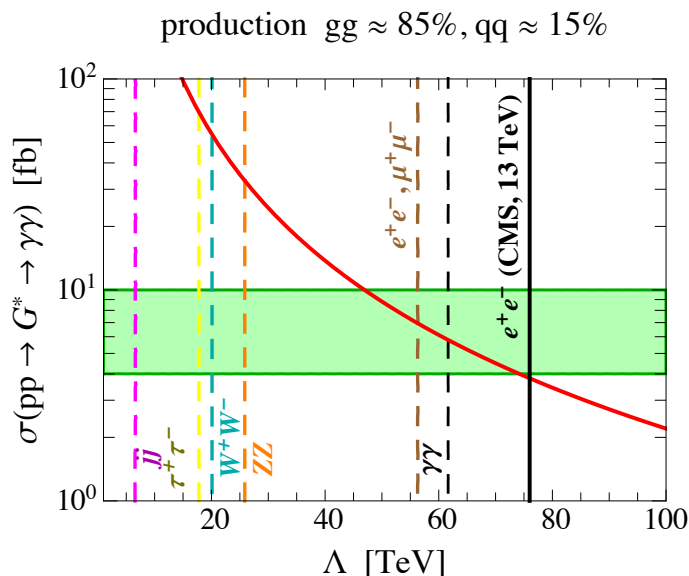


FIG. 14: *Parameter space for the lightest KK spin-2 graviton excitation G^* . We show in red the di-photon cross-section $\sigma(pp \rightarrow G^* \rightarrow \gamma\gamma)$ at $\sqrt{s} = 13$ TeV as a function of the effective scale Λ . The vertical dashed lines mark the regions excluded at $\sqrt{s} = 8$ TeV. The vertical solid line corresponds to the CMS bound from e^+e^- final state at $\sqrt{s} = 13$ TeV [25]. The green band reproduces the cross-section $\sigma(pp \rightarrow G^* \rightarrow \gamma\gamma) = [4 - 10]$ fb.*

searches for di-lepton decay of a spin-1 resonance but they can be recast for the case of the KK graviton as shown in [25]. The e^+e^- di-lepton final state in CMS put the constraint $\Lambda > 76$ TeV. The latter shows some tension with the signal strength needed to fit the di-photon excess at $\sqrt{s} = 13$ TeV.

Given the current uncertainties in the actual value of the signal strength needed to reproduced the observed excess, no strong conclusions can be derived from these bounds.² Nevertheless, it goes without saying that if the di-photon excess will be confirmed in the next future, the explanation in terms of the lightest KK graviton excitation can be

² In [1] the CMS collaboration presented a combined fit of di-photon data at at $\sqrt{s} = 8$ and $\sqrt{s} = 13$ TeV, and the reported best-fit value is $\sigma(pp \rightarrow G^* \rightarrow \gamma\gamma) = 4.5^{+1.9}_{-1.7}$ fb ($\Lambda = 86^{+20}_{-17}$ TeV) that is compatible with the di-lepton bound. Notice that our analysis does not depend on the specific value of Λ assumed, since it cancels out from the normalised pdf of the signal.

ruled out in the absence of a corresponding bump in the di-lepton spectrum. Keeping this discussion in mind, in the rest of this section we explore the KK graviton example for our spin-2 analysis.

As far as the production mechanism is concerned, we find that gluon fusion accounts for about 85% of the total rate while $q\bar{q}$ annihilation is responsible for the remaining 15%. This is an important point, since it means that the angular distribution in eq. (5) is contaminated by the one in eq. (6). The results presented in section V—strictly valid only in the case of production via gluon fusion—are therefore non longer applicable to a KK graviton, and a dedicated analysis is needed.

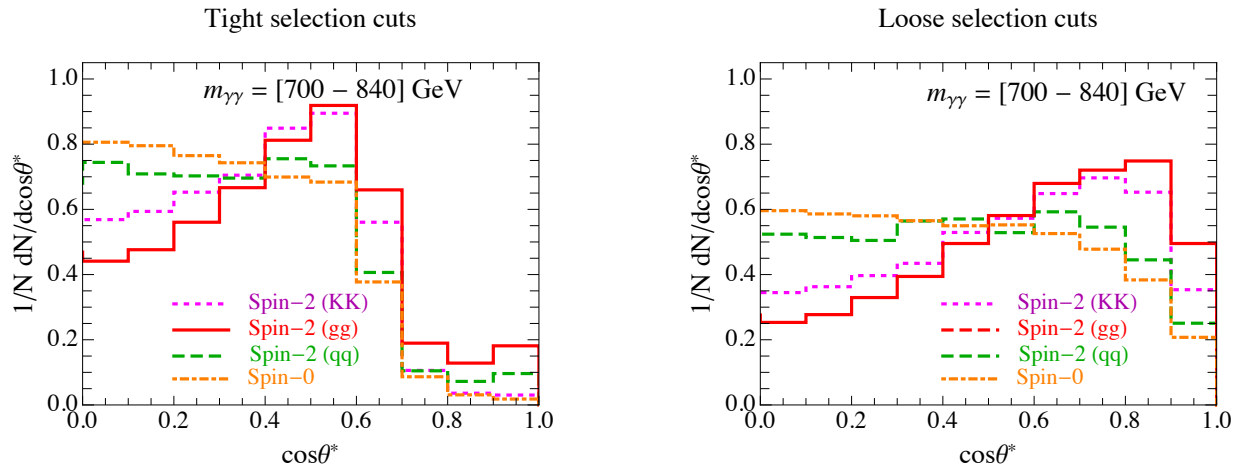


FIG. 15: Comparison between the angular distribution for the signal events. Dot-dashed orange: spin-0 resonance; solid red: spin-2 resonance produced via gluon fusion; dashed green: spin-2 resonance mostly produced via $q\bar{q}$; dotted magenta: spin-2 KK graviton with universal couplings. We show the case with tight selection cuts in the left panel, and the analysis with loose selection cuts in the right one.

Following the same framework of section IV and V, we show in fig. 15 the angular distributions for the signal samples corresponding to tight cuts (left panel) and loose cuts (right panel). In addition to the spin-2 resonance produced via gluon fusion (solid red) and the spin-0 case (dot-dashed orange) discussed in section V, we show in dotted magenta the angular distribution for the KK graviton and in dashed green the case of a spin-2 resonance mostly produced by $q\bar{q}$ annihilation (we shall discuss this case in more detail in the next section). These angular distributions reflect what already expected from our general discussion. The 15% $q\bar{q}$ contamination for a KK graviton sizeably alters the pdf generated by gluon fusion. As evident from the comparison with the dashed green line, the larger the $q\bar{q}$ contamination the closer the result to the spin-0 case. It is now important to quantify this effect in terms of significance.

In fig. 16 we show our results for the center-edge asymmetry. For the sake of simplicity we consider only signal events. We compare the distributions for the four cases proposed in fig. 15. For both tight (left panel) and loose (right panel) cuts the KK graviton distribution shifts towards the spin-0 one if compared with the results of section V. The reduced distance between the two cases corresponds to a lower separation in terms of statistical significance. Similar results can be obtained by means of the LLR.

The main result of this section is summarised in fig. 17. We show the significance \mathcal{Z} as a function of the collected number of events. As in fig. 13 we compare the results obtained using the LLR and the center-edge/dartboard asymmetry (see caption and labels for details).

On the qualitative level our findings are similar to those already discussed in section V. Loose cuts perform slightly better than tight ones, and the LLR gives better result than the center-edge asymmetry. Considering only signal events (left panel in fig. 17) and loose cuts a significance of $\mathcal{Z} \simeq 3$ ($\mathcal{Z} \simeq 4$) can be reached with $N_{\text{obs}}^{(J)} = 20$ ($N_{\text{obs}}^{(J)} = 100$) events, and slightly worse results—significance of $\mathcal{Z} \simeq 2$ ($\mathcal{Z} \simeq 3$) with $N_{\text{obs}}^{(J)} = 20$ ($N_{\text{obs}}^{(J)} = 100$) events—are possible by imposing tight selection cuts. The inclusion of background events reduces the expected significance. In the extreme case in which we include in our simulated samples an equal number of signal and background events (right panel in fig. 17) we expect at most a $\mathcal{Z} \simeq 3$ significance for the spin-2 KK graviton hypothesis with loose selection cuts and $N_{\text{obs}}^{(J)} = N_{\text{obs}}^{(\text{bkg})} = 100$.

The significance $\mathcal{Z} = 3$ threshold is reached for 70 (140) events for the signal with loose (tight) selection cuts. The situation is therefore different from before for the case of a spin-2 resonance produced only by gluon fusion. The choice of selection cuts makes a difference and a luminosity of about 9 fb^{-1} is necessary in the case of the loose cuts whereas a larger luminosity of 25 fb^{-1} is required by the tight selection cuts.

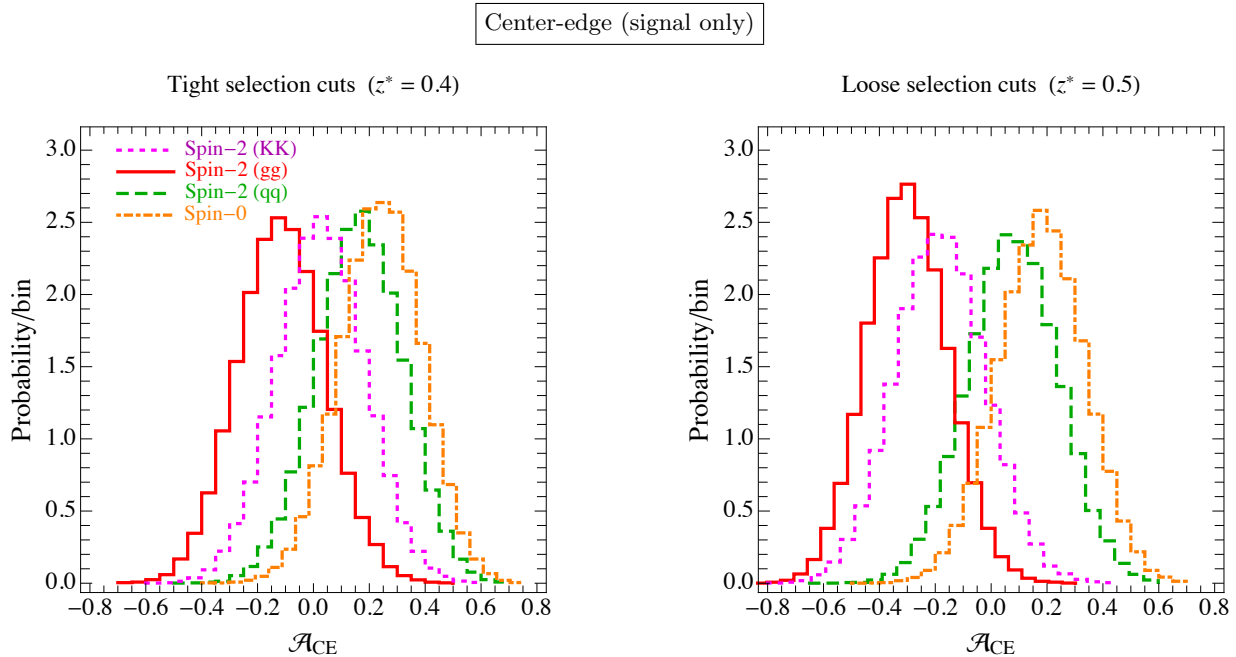


FIG. 16: The same as in fig. 12 but including also the central-edge asymmetry for the KK graviton (dotted magenta) and the case of a spin-2 resonance mostly produced via $q\bar{q}$ (dashed green).

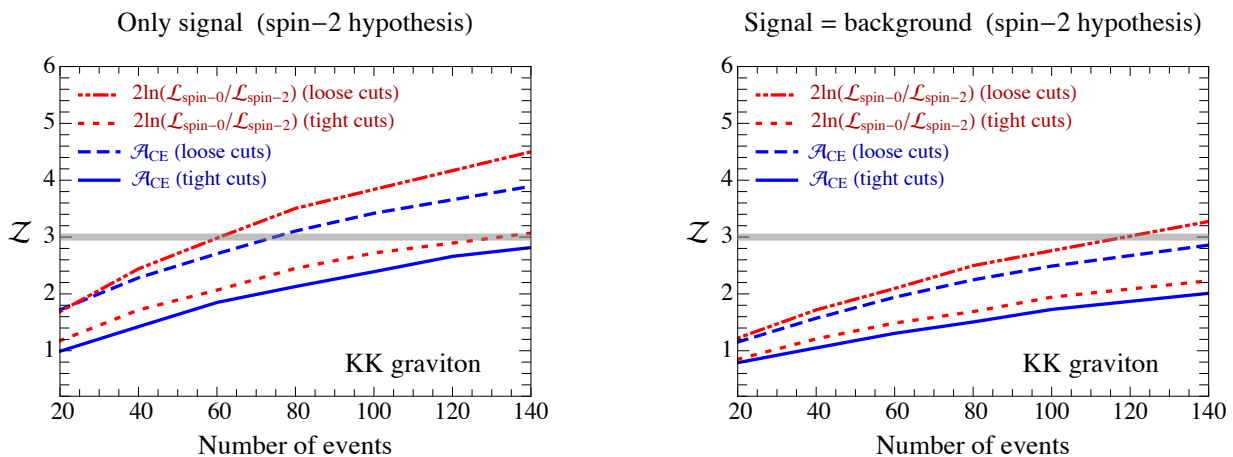


FIG. 17: Significance \mathcal{Z} for the LLR and the center-edge asymmetry as a function of the number of events. The significance refers to the spin-2 hypothesis in the case of a KK graviton with universal couplings.

A. Estimating the model-dependent systematic uncertainty

The presence of the $q\bar{q}$ production mechanism reduces the discriminating power of the angular distributions. For the case of the KK gravitons, we find a reduction of the significance \mathcal{Z} of the order of 10%-30% (depending on the analysis) with respect to the case in which the spin-2 resonance is produced only via gluon fusion.

A more significant reduction takes place if the $q\bar{q}$ production mechanism becomes more important. Fig. 16 shows the reduced discrimination power as the $q\bar{q}$ production becomes the dominant one. This reduction in significance is due to a systematic error intrinsic to the definition of the model behind the spin-2 hypothesis in so far as the angular distribution depends on the production mechanism.

The case in which the $q\bar{q}$ production mechanism is dominant requires a larger number of events in order to tell the two spin possibilities apart. Fig. 18 shows the significance in the extreme case (still compatible with other experimental constraints) of $q\bar{q}$ accounting for 80% of the production.

In this case, it is not possible to reach the $\mathcal{Z} = 3$ level with a reasonable number of events and one must include

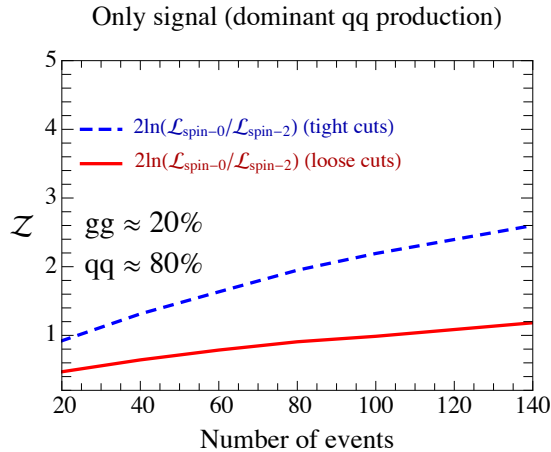


FIG. 18: Significance Z for the LLR as a function of the number of events. In the model for the spin-2 resonance, the production mechanism is taken to be dominated by $q\bar{q}$ production.

in the analysis other decay channels. For the case of the Higgs boson, it has been shown [3] that the decay channel into two W gauge bosons enjoys an angular variable that is less sensitive to the production mechanism. This channel, together with that into two Z bosons, can also be used to distinguish the parity of the resonance. We postpone such an analysis to a time after the existence of the resonance has been ascertained.

Finally, one must bear in mind that many other systematic errors—for example, those on the integrated luminosity and selection efficiency or those on the photon identification—are lurking around different steps of the analysis. Their impact could in principle be estimated by incorporating the uncertainties into the likelihoods or convoluting the pdf with the corresponding *nuisance* parameters. We have not attempted such a procedure here because a realistic estimate of these uncertainties can only be done by the experimental collaborations.

Acknowledgments

We thank Roberto Franceschini, Nicola Orlando and Alberto Tonero for discussions. MF thanks the International School for Advanced Studies (SISSA) and the Physics Department of the University of Trieste for the hospitality.

Appendix A: Comparison with the ATLAS results

The ATLAS collaboration presented two analysis: the first one—dubbed “spin-0 analysis” in [10], and shown in the left panel of fig. 19—is optimised for a spin-0 resonance search while the second one—dubbed “spin-2 analysis” in [10], and shown in the right panel of fig. 19—is optimised for a spin-2 resonance search. In this paper, the analysis with tight (loose) selection cuts corresponds to the “spin-0 analysis” (“spin-2 analysis”) in [10]. In both cases we superimpose to the experimental data (representing the full data set, without any background subtraction) the pdfs for the signal-plus-background events generated in section V for both the spin-0 and spin-2 case. For the “spin-0 analysis” (“spin-2 analysis”) resonance search, 31 (70) data events are observed with $m_{\gamma\gamma} = [700 - 840]$ GeV [10].

Let us start considering the “spin-0 analysis”. The fit of the mass-invariant spectrum is shown in fig. 1, and from our best-fit values in table I we find $N_{\text{obs}}^{(J)} = 18.0$ signal and $N_{\text{obs}}^{(\text{bkg})} = 12.4$ background events—in agreement with the total value of 31 events quoted by the ATLAS collaboration. We therefore apply the LLR analysis outlined in section VB, simulating $N_{ps} = 10^4$ pseudo-experiments with $N_{\text{obs}}^{(J)} = 18$ signal and $N_{\text{obs}}^{(\text{bkg})} = 12$ background events. We use tight selection cuts since they are equivalent—as stated above—to the “spin-0 analysis”. We show our results in fig. 20 where we compare the spin-0 hypothesis with both the spin-2 produced via gluon fusion and the KK graviton (respectively, in the left and right panel).

Even though it is not possible to derive any definite conclusions from these very preliminary results, it is interesting to try an hypothesis testing. Assuming the spin-0 nature of the resonance—that is sitting on the median of the corresponding distribution, see fig. 20—we can estimate the statistical significance of this choice by computing the probability to accept the spin-0 hypothesis when it is wrong (that is, an error of Type I represented by the red and magenta regions in fig. 20). Alternatively, one can do the opposite assuming the spin-2 nature of the resonance. As far

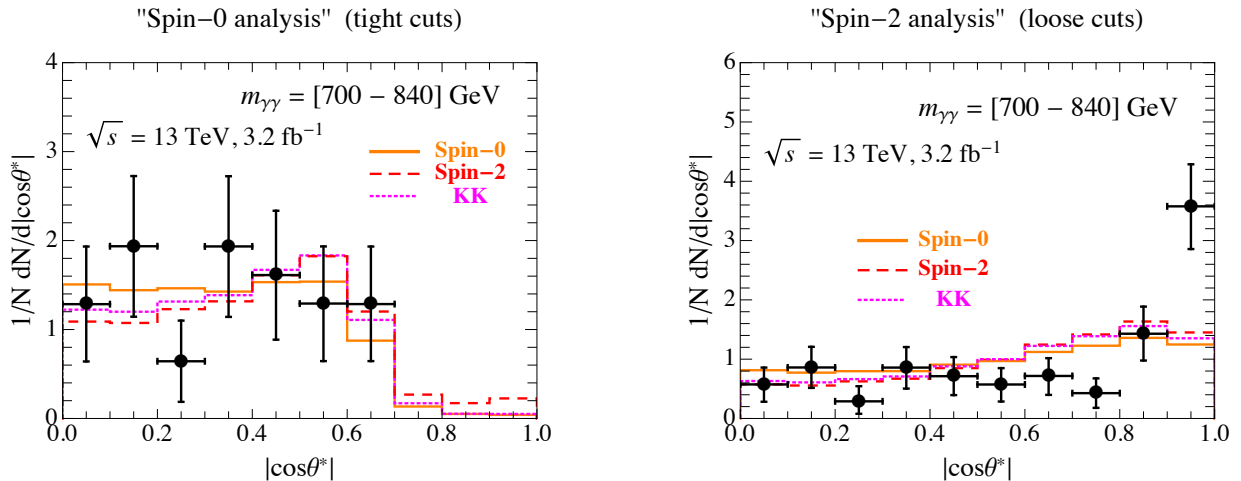


FIG. 19: Distribution of $|\cos\theta^*|$ for events in the mass interval $m_{\gamma\gamma} = [700 - 840]$ GeV. Data points are digitalised from the ATLAS reference in [10]. We superimpose the distributions for the signal-plus-background events generated in section V for both the spin-0 and spin-2 case. Signal and background distributions are weighted in such a way to reproduce $N_{\text{obs}}^{(J)} = 18$ signal and $N_{\text{obs}}^{(\text{bkg})} = 12$ background events for the “spin-0 analysis” (left panel) and $N_{\text{obs}}^{(J)} = 25$ signal and $N_{\text{obs}}^{(\text{bkg})} = 45$ background events for the “spin-2 analysis” (right panel).

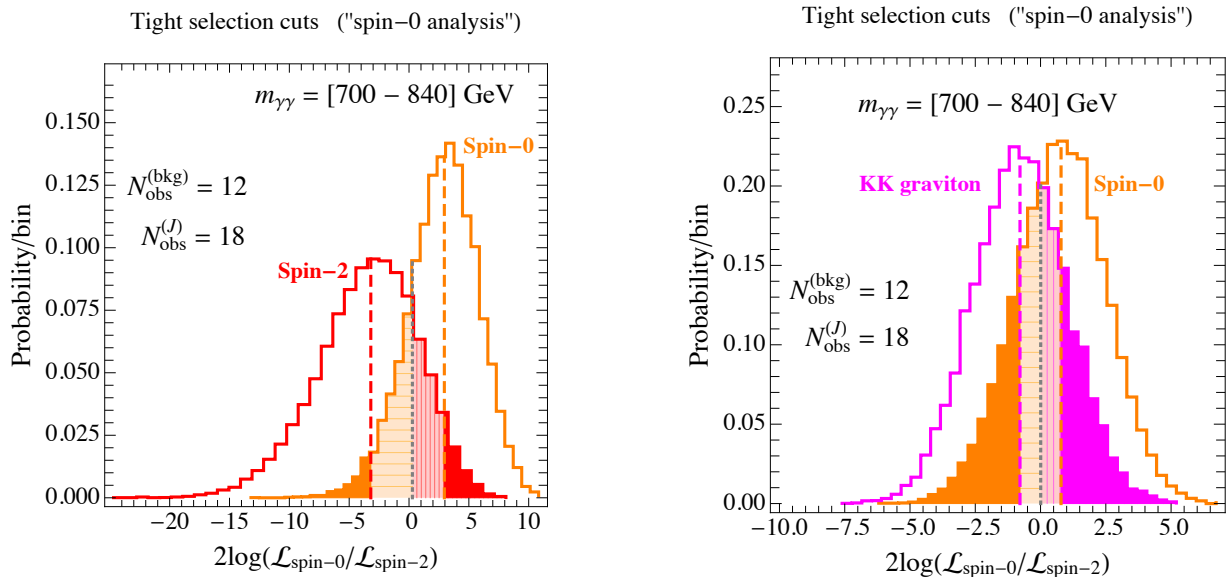


FIG. 20: LLR analysis for $N_{\text{obs}}^{(J)} = 18$ signal and $N_{\text{obs}}^{(\text{bkg})} = 12$ background events. In the left (right) panel we compare the spin-2 produced via gluon fusion (KK graviton) and spin-0 hypotheses. The vertical dashed lines represent the medians of the two distributions (see also caption of fig. 11).

as the case with the KK graviton is concerned, as clear from the right panel of fig. 20 it is not possible to derive any conclusion since the two hypothesis are equally preferred by the LLR analysis. Considering the left panel of fig. 20, on the contrary, we find the p -value $P_2 \simeq 0.048$ for the spin-0 hypothesis, corresponding to the statistical significance $\mathcal{Z} \simeq 1.66$. Assuming the spin-2 hypothesis, we find the p -value $P_0 \simeq 0.028$, corresponding to the statistical significance $\mathcal{Z} \simeq 1.89$. We find similar results taking into account the “spin-2 analysis” with $N_{\text{obs}}^{(J)} = 25$ signal and $N_{\text{obs}}^{(\text{bkg})} = 45$ background events (we do not show the corresponding distributions, qualitatively equivalent to the one shown in fig. 20). Considering the case with the spin-2 resonance produced via gluon fusion, we find the p -value $P_2 \simeq 0.047$ for the spin-0 hypothesis, corresponding to the statistical significance $\mathcal{Z} \simeq 1.67$. Assuming the spin-2 hypothesis, we find the p -value $P_0 \simeq 0.033$, corresponding to the statistical significance $\mathcal{Z} \simeq 1.83$.

Finally, by looking at the result of the “spin-2 analysis” in the right panel of fig. 19, the presence of a discrepancy in the last few bins catches the eye. As far as the analysis with loose selection cuts (or, equivalently, the “spin-2

analysis” in [10]) is concerned, we do not find any particular peak in the forward region with $|\cos\theta^*| > 0.8$ even in the presence of a spin-2 signal compatible in strength with the observed excess. This is expected, since the forward region is depleted by limited detector acceptances. Of course one may argue that our phenomenological analysis cannot reproduce the same accuracy in photon identification and isolation reached by the experimental analysis; despite being this objection very true, the presence of similar discrepancies in the forward region also in the sidebands with $m_{\gamma\gamma} = [600 - 700]$ GeV and $m_{\gamma\gamma} = [840 - \infty]$ GeV (see the corresponding plots in [10]) seems to point towards the existence of some uncontrolled systematics.

Bearing all this in mind, let us entertain the possibility that the discrepancy in the forward region is actually due to the presence of a spin-2 signal. It follows that this effect, if real, should be related to something that is not captured by the simulated signal-plus-background events. One intriguing possibility is represented by non-trivial interference effects between the spin-2 signal and the SM background. We discuss this case in the next sub-section.

1. Resonance-continuum interference for a spin-2 state

The interference between resonance and continuum—that is the interference between diagrams D and E in fig. 4—cannot be neglected in the di-photon Higgs signal at the LHC, as pointed out in [7]. In [28] the analysis was extended for the di-photon excess at 750 GeV but only in the case of a scalar resonance. Let us focus on the relevant points of the computation. We consider production via gluon fusion of a resonance with mass M_X and width Γ_X . At the parton level with center of mass \hat{s} the amplitude is

$$\mathcal{A}_{gg\rightarrow\gamma\gamma} = -\frac{\mathcal{A}_{gg\rightarrow X}\mathcal{A}_{X\rightarrow\gamma\gamma}}{\hat{s} - M_X^2 + iM_X\Gamma_X} + \mathcal{A}_{\text{cont}} , \quad (\text{A1})$$

where $\mathcal{A}_{\text{cont}}$ is the amplitude for the background process generated by gluon fusion while $\mathcal{A}_{gg\rightarrow X}$ and $\mathcal{A}_{X\rightarrow\gamma\gamma}$ are the amplitude for the production of X and the subsequent di-photon decay. In the SM the amplitude $\mathcal{A}_{\text{cont}}$ arises at one-loop level (see fig. 4). The interference term is [7]

$$\delta\hat{\sigma}_{gg\rightarrow X\rightarrow\gamma\gamma} = -2(\hat{s} - M_X^2) \frac{\text{Re}(\mathcal{A}_{gg\rightarrow X}\mathcal{A}_{X\rightarrow\gamma\gamma}\mathcal{A}_{\text{cont}}^*)}{(\hat{s} - M_X^2)^2 + M_X^2\Gamma_X^2} - 2M_X\Gamma_X \frac{\text{Im}(\mathcal{A}_{gg\rightarrow X}\mathcal{A}_{X\rightarrow\gamma\gamma}\mathcal{A}_{\text{cont}}^*)}{(\hat{s} - M_X^2)^2 + M_X^2\Gamma_X^2} , \quad (\text{A2})$$

and the corresponding contribution at the hadron level is

$$\delta\sigma_{pp\rightarrow X\rightarrow\gamma\gamma} = \int \frac{d\hat{s}}{\hat{s}} \frac{dL_{gg}}{d\hat{s}} \delta\hat{\sigma}_{gg\rightarrow X\rightarrow\gamma\gamma} , \quad (\text{A3})$$

with $dL_{gg}/d\hat{s}$ the gluon luminosity function. We start briefly discussing the case of the Higgs boson. The first term in eq. (A2) turns out to be zero in the narrow-width approximation when integrated over an invariant-mass bin centered on the resonance. The second term in eq. (A2) needs a large imaginary part to give a sizeable contribution. For the Higgs, the largest imaginary contribution arises at two-loop level from the background $gg \rightarrow \gamma\gamma$ amplitude (at one loop the spin-0 nature of the Higgs boson selects, as a consequence of helicity conservation, only the like-helicity states $g^\pm g^\pm$ and $\gamma^\pm \gamma^\pm$ whose amplitudes are suppressed by the factor m_q^2/m_H^2 [17]). Despite the two-loop suppression, for a Higgs boson the resonance-continuum interference generates non-negligible effects in particular in the forward direction.

Motivated by this observation, it would be interesting—if the di-photon excess will be confirmed in the near future with a persisting discrepancy in the forward direction—to generalise the analysis to the case of a spin-2 resonance. In the following we only list some differences with respect to the case of the spin-0 Higgs:

- If the hint in favor of a broad resonance ($\Gamma_X \sim 6\% M_X$) will be confirmed, the narrow-width approximation is no longer applicable to the first term in eq. (A2). As discussed in [28], the net effect of this term is a distortion of the shape of the resonance.
- The term proportional to the imaginary part in eq. (A2) is proportional to the width Γ_X , and it is enhanced in the large-width scenario. Furthermore, contrary to the Higgs case, a large imaginary part in $\mathcal{A}_{gg\rightarrow X}\mathcal{A}_{X\rightarrow\gamma\gamma}\mathcal{A}_{\text{cont}}^*$ may be generated in $\mathcal{A}_{gg\rightarrow X}$ and $\mathcal{A}_{X\rightarrow\gamma\gamma}$ if $M_X > 2M_V$, where M_V generically denotes the mass of the particles—either SM, like the W or the top, or new vector-like states—running in the loop.
- As far as the imaginary part coming from $\mathcal{A}_{\text{cont}}^*$ is concerned, as mentioned before in the case of a spin-0 resonance one is forced to consider only amplitudes with like-helicity states $g^\pm g^\pm$ and $\gamma^\pm \gamma^\pm$ that are purely real. In the case of a spin-2 particle, on the contrary, this selection rule is no longer valid since all possible

helicity combinations are allowed. One may therefore get a large contribution already at one loop by overcoming the mass suppression m_q^2/m_H^2 characteristic of the scalar Higgs case.

The helicity structure of the one-loop process $gg \rightarrow \gamma\gamma$ was studied in [17]. There are 16 helicity structures $\mathcal{A}_{\lambda_1\lambda_2\rightarrow\lambda_3\lambda_4}(s, t, u)$ contributing to $\mathcal{A}_{\text{cont}}$, where $\lambda_{1,2}$ and $\lambda_{3,4}$ denote, respectively, the helicities of the incoming gluons and outgoing photons, and s, t, u are the usual Mandelstam variables for the scattering process $gg \rightarrow \gamma\gamma$. Only three of them are really needed to reconstruct the full amplitude, since all the remaining ones can be derived using crossing relations, parity and permutation symmetry.

Following [17], we focus on $\mathcal{A}_{++++}(s, t, u)$, $\mathcal{A}_{+++-}(s, t, u)$, and $\mathcal{A}_{+--+}(s, t, u)$. In the massless limit for the quarks running in the box diagram, the only imaginary part with like-helicity states—relevant for the interference with a spin-0 resonance—is [17]

$$\text{Im}[\mathcal{A}_{++++}(s, t, u)] = -\pi[\vartheta(t) - \vartheta(u)] \times \left[\frac{t-u}{s} + \frac{t^2+u^2}{s^2} \log\left|\frac{t}{u}\right| \right], \quad (\text{A4})$$

that however vanishes since $t = -(s/2)(1 - \cos\theta) < 0$, $u = -(s/2)(1 + \cos\theta) < 0$, with θ the scattering angle in the center of mass frame.

In the presence of a spin-2 resonance, the interference involves amplitudes with different helicities in the initial and final state. Using crossing symmetry, we find

$$\text{Im}[\mathcal{A}_{+--+}(s, t, u)] = -\pi[\vartheta(t) - \vartheta(s)] \times \left[\frac{t-s}{u} + \frac{t^2+s^2}{u^2} \log\left|\frac{t}{s}\right| \right], \quad (\text{A5})$$

$$\text{Im}[\mathcal{A}_{-+-+}(s, t, u)] = -\pi[\vartheta(s) - \vartheta(u)] \times \left[\frac{s-u}{t} + \frac{s^2+u^2}{t^2} \log\left|\frac{s}{u}\right| \right], \quad (\text{A6})$$

This very simple computation shows that in the presence of a spin-2 resonance large imaginary contributions from the continuum part in the second term of eq. (A2) are possible: they are described by the amplitudes in eqs. (A5, A6), and they are not suppressed by the quark masses.

- Finally, it is important to keep in mind another important difference with respect to the Higgs case. Let us consider the various diagrams participating in the definition of the irreducible SM background, depicted in fig. 4. In the invariant mass range $m_{\gamma\gamma} = [100 - 200]$ GeV—relevant for di-photon Higgs searches—the one-loop amplitude $gg \rightarrow \gamma\gamma$ is comparable in size with the tree-level non-resonant di-photon process $q\bar{q} \rightarrow \gamma\gamma$. This is no longer true in the mass range $m_{\gamma\gamma} = [700 - 840]$ GeV where the one-loop amplitude $gg \rightarrow \gamma\gamma$ turns out to be one order of magnitude smaller than the tree-level process $q\bar{q} \rightarrow \gamma\gamma$, as shown in fig. 21. As a result, resonant-continuum interference involving the one-loop amplitude $gg \rightarrow \gamma\gamma$ has to overcome this large suppression in order to give a sizeable correction to the di-photon signal rate.

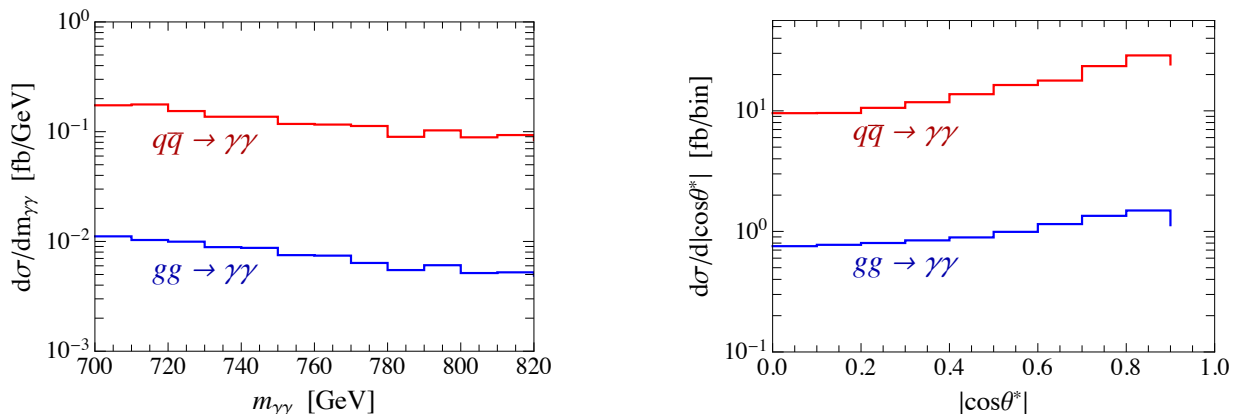


FIG. 21: Comparison between the tree level cross-section $q\bar{q} \rightarrow \gamma\gamma$ (red) and the one loop process $gg \rightarrow \gamma\gamma$ (blue) at the LHC with $\sqrt{s} = 13$ TeV. We show in the left panel the differential cross-section $d\sigma/dm_{\gamma\gamma}$ as a function of the di-photon invariant mass, and in the right panel the differential cross-section $d\sigma/d|\cos\theta^*|$ as a function of the scattering angle in the CS frame (see fig. 2). In the right panel we include only events with $m_{\gamma\gamma} = [700 - 840]$ GeV.

-
- [1] ATLAS collaboration, [ATLAS-CONF-2015-081](#); CMS collaboration, [CMS-PAS-EXO-15-004](#).
- [2] D. J. Miller, S. Y. Choi, B. Eberle, M. M. Muhlleitner and P. M. Zerwas, Phys. Lett. B **505**, 149 (2001) [[hep-ph/0102023](#)]; Y. Gao, A. V. Gritsan, Z. Guo, K. Melnikov, M. Schulze and N. V. Tran, Phys. Rev. D **81**, 075022 (2010) [[arXiv:1001.3396](#) [hep-ph]]; A. De Rujula, J. Lykken, M. Pierini, C. Rogan and M. Spiropulu, Phys. Rev. D **82**, 013003 (2010) [[arXiv:1001.5300](#) [hep-ph]]; U. De Sanctis, M. Fabbrichesi and A. Tonerò, Phys. Rev. D **84**, 015013 (2011) [[arXiv:1103.1973](#) [hep-ph]]; A. Alves, Phys. Rev. D **86**, 113010 (2012) [[arXiv:1209.1037](#) [hep-ph]]; S. Y. Choi, M. M. Muhlleitner and P. M. Zerwas, Phys. Lett. B **718**, 1031 (2013) [[arXiv:1209.5268](#) [hep-ph]].
- [3] G. Aad *et al.* [ATLAS Collaboration], Phys. Lett. B **726**, 120 (2013) [[arXiv:1307.1432](#) [hep-ex]]; S. Chatrchyan *et al.* [CMS Collaboration], Phys. Rev. D **89**, no. 9, 092007 (2014) [[arXiv:1312.5353](#) [hep-ex]].
- [4] L. D. Landau, Dokl. Akad. Nauk Ser. Fiz. **60**, no. 2, 207 (1948); C. N. Yang, Phys. Rev. **77**, 242 (1950).
- [5] M. Pivk and F. R. Le Diberder, Nucl. Instrum. Meth. A **555**, 356 (2005) [[physics/0402083](#) [physics.data-an]].
- [6] E. W. Dvergsnes, P. Osland, A. A. Pankov and N. Paver, Phys. Rev. D **69**, 115001 (2004) [[hep-ph/0401199](#)]; P. Osland, A. A. Pankov and N. Paver, Phys. Rev. D **68**, 015007 (2003) [[hep-ph/0304123](#)]; P. Osland, A. A. Pankov and A. V. Tsytin, Eur. Phys. J. C **75** (2015) no.5, 199 [[arXiv:1410.4942](#) [hep-ph]].
- [7] L. J. Dixon and M. S. Siu, Phys. Rev. Lett. **90**, 252001 (2003) [[hep-ph/0302233](#)]; L. J. Dixon and Y. Sofianatos, Phys. Rev. D **79**, 033002 (2009) [[arXiv:0812.3712](#) [hep-ph]].
- [8] G. Panico, L. Vecchi and A. Wulzer, [arXiv:1603.04248](#) [hep-ph].
- [9] J. Bernon, A. Goudelis, S. Kraml, K. Mawatari and D. Sengupta, [arXiv:1603.03421](#) [hep-ph].
- [10] The ATLAS collaboration, *Search for resonances in diphoton events with the ATLAS detector at $\sqrt{s} = 13$ TeV*, [ATLAS-CONF-2016-018](#); *Diphoton searches in ATLAS*, talk at Rencontres de Moriond 2016, Electroweak interactions and unified theories [[SLIDES](#)].
- [11] CMS Collaboration, [CMS-PAS-EXO-16-018](#).
- [12] R. Franceschini *et al.*, JHEP **1603**, 144 (2016) [[arXiv:1512.04933](#) [hep-ph]].
- [13] S. Knapen, T. Melia, M. Papucci and K. Zurek, [arXiv:1512.04928](#) [hep-ph].
- [14] L. Randall and R. Sundrum, Phys. Rev. Lett. **83**, 3370 (1999) [[hep-ph/9905221](#)].
- [15] J. C. Collins and D. E. Soper, Phys. Rev. D **16**, 2219 (1977).
- [16] G. F. Giudice, R. Rattazzi and J. D. Wells, Nucl. Phys. B **544**, 3 (1999) [[hep-ph/9811291](#)]; T. Han, J. D. Lykken and R. J. Zhang, Phys. Rev. D **59** (1999) 105006 [[hep-ph/9811350](#)]; K. Hagiwara, J. Kanzaki, Q. Li and K. Mawatari, Eur. Phys. J. C **56** (2008) 435 [[arXiv:0805.2554](#) [hep-ph]].
- [17] D. A. Dicus and S. S. D. Willenbrock, Phys. Rev. D **37**, 1801 (1988).
- [18] A. Alloul, N. D. Christensen, C. Degrande, C. Duhr and B. Fuks, Comput. Phys. Commun. **185**, 2250 (2014) [[arXiv:1310.1921](#) [hep-ph]]; [FeynRules](#).
- [19] P. Artoisenet *et al.*, JHEP **1311**, 043 (2013) [[arXiv:1306.6464](#) [hep-ph]]; [The Higgs characterization model](#).
- [20] J. Alwall *et al.*, JHEP **1407** (2014) 079 [[arXiv:1405.0301](#) [hep-ph]]; [MadGraph5_aMC@NLO web site](#).
- [21] T. Sjostrand, S. Mrenna and P. Z. Skands, JHEP **0605** (2006) 026 [[hep-ph/0603175](#)]; [Pythia 6 web site](#).
- [22] J. de Favereau *et al.* [DELPHES 3 Collaboration], JHEP **1402** (2014) 057 [[arXiv:1307.6346](#) [hep-ex]]; [Delphes web site](#).
- [23] R. Brun and F. Rademakers, Nucl. Instrum. Meth. A **389**, 81 (1997); [Root web site](#).
- [24] J. Neyman and E. S. Pearson, Phil. Trans. R. Soc. A231 (1933) 289.
- [25] S. B. Giddings and H. Zhang, [arXiv:1602.02793](#) [hep-ph].
- [26] A. Carmona, [arXiv:1603.08913](#) [hep-ph]; A. Falkowski and J. F. Kamenik, [arXiv:1603.06980](#) [hep-ph]; J. L. Hewett and T. G. Rizzo, [arXiv:1603.08250](#) [hep-ph]; B. M. Dillon and V. Sanz, [arXiv:1603.09550](#) [hep-ph].
- [27] The ATLAS collaboration, [ATLAS-CONF-2015-070](#); the CMS Collaboration, [CMS-PAS-EXO-15-005](#).
- [28] S. Jung, J. Song and Y. W. Yoon, [arXiv:1601.00006](#) [hep-ph].